






ORIGINAL RESEARCH

Myocardial Iron Deficiency and Mitochondrial Dysfunction in Advanced Heart Failure in Humans

Hao Zhang, MD; K. Lockhart Jamieson , PhD; Justin Grenier , MSc; Anish Nikhanj, MSc; Zeyu Tang, MD; Faqi Wang, PhD; Shaohua Wang, MD, MSc; Jonathan G. Seidman , PhD; Christine E. Seidman , MD; Richard Thompson, PhD; John M. Seubert, PhD; Gavin Y. Oudit , MD, PhD

BACKGROUND: Myocardial iron deficiency (MID) in heart failure (HF) remains largely unexplored. We aim to establish defining criterion for MID, evaluate its pathophysiological role, and evaluate the applicability of monitoring it non-invasively in human explanted hearts.

METHODS AND RESULTS: Biventricular tissue iron levels were measured in both failing (n=138) and non-failing control (NFC, n=46) explanted human hearts. Clinical phenotyping was complemented with comprehensive assessment of myocardial remodeling and mitochondrial functional profiles, including metabolic and oxidative stress. Myocardial iron status was further investigated by cardiac magnetic resonance imaging. Myocardial iron content in the left ventricle was lower in HF versus NFC (121.4 [88.1–150.3] versus 137.4 [109.2–165.9] $\mu\text{g/g}$ dry weight), which was absent in the right ventricle. With a priori cutoff of 86.1 $\mu\text{g/g}$ d.w. in left ventricle, we identified 23% of HF patients with MID (HF-MID) associated with higher NYHA class and worsened left ventricle function. Respiratory chain and Krebs cycle enzymatic activities were suppressed and strongly correlated with depleted iron stores in HF-MID hearts. Defenses against oxidative stress were severely impaired in association with worsened adverse remodeling in iron-deficient hearts. Mechanistically, iron uptake pathways were impeded in HF-MID including decreased translocation to the sarcolemma, while transmembrane fraction of ferroportin positively correlated with MID. Cardiac magnetic resonance with T2* effectively captured myocardial iron levels in failing hearts.

CONCLUSIONS: MID is highly prevalent in advanced human HF and exacerbates pathological remodeling in HF driven primarily by dysfunctional mitochondria and increased oxidative stress in the left ventricle. Cardiac magnetic resonance demonstrates clinical potential to non-invasively monitor MID.

Key Words: cardiac magnetic resonance imaging ■ heart failure ■ iron transporters ■ mitochondria ■ myocardial iron deficiency

Heat failure (HF) remains extremely prevalent on a global scale with high morbidity and mortality.^{1,2} Comorbid conditions in patients with advanced HF not only complicate the presentation and treatment, but also play an instrumental role in progression of HF.³ Thus, management of comorbidities is gaining equal importance to treating the primary cause of HF itself.^{2,4} Iron deficiency (ID) is the most common malnutrition globally, and often co-exists with HF irrespective of

the presence of abnormal blood cell indices (i.e., anemia).^{5,6} Conventionally, systemic iron deficiency (SID), defined as either absolute deficit with serum ferritin <100 $\mu\text{g/L}$ or functional insufficiency combining serum ferritin 100–300 $\mu\text{g/L}$ and transferrin saturation <20%, represents ID in the context of HF.^{3,6–8} Prior studies have demonstrated the detrimental impact of SID on patients' physical capacity and clinical outcomes,^{5,9} whereas iron supplementations exhibited substantial

Correspondence to: Gavin Y. Oudit, MD, PhD, FRCP(C), Division of Cardiology, Department of Medicine, Mazankowski Alberta Heart Institute, University of Alberta, Edmonton, Alberta, Canada, T6G 2S2. Email: gavin.oudit@ualberta.ca

Supplemental Material for this article is available at <https://www.ahajournals.org/doi/suppl/10.1161/JAHA.121.022853>

For Sources of Funding and Disclosures, see page 16.

© 2022 The Authors. Published on behalf of the American Heart Association, Inc., by Wiley. This is an open access article under the terms of the [Creative Commons Attribution-NonCommercial-NoDerivs](https://creativecommons.org/licenses/by-nc-nd/4.0/) License, which permits use and distribution in any medium, provided the original work is properly cited, the use is non-commercial and no modifications or adaptations are made.

JAHA is available at: www.ahajournals.org/journal/jaha

CLINICAL PERSPECTIVE

What Is New?

- Myocardial iron deficiency is common in explanted failing human hearts with either dilated cardiomyopathy or coronary artery disease.
- Myocardial iron deficiency correlated with greater adverse myocardial remodeling, oxidative stress, and suboptimal mitochondrial structure and function.
- Myocardial iron deficiency correlated with reduced levels of iron importers, transferrin receptor-1 and divalent metal transporter-1, and increased levels of the sole iron exporter, ferroportin, in the sarcolemma.

What Are the Clinical Implications?

- Magnetic resonance imaging can detect myocardial iron deficiency.
- Iron supplementation in patients with myocardial iron deficiency, in the absence of major systemic iron deficiency and anemia, is a potential therapy for patients with advanced heart failure.

NYHA

New York Heart Association Classification

ROS

reactive oxygen species

SID

systemic iron deficiency

SOD

superoxide dismutase

TEM

transmission electron microscopy

TFR-1

transferrin receptor 1

Nonstandard Abbreviations and Acronyms

CAT	catalase
COX I/II/III/IV	Complexes I/II/III/IV
CS	citrate synthase
DCM	dilated cardiomyopathy
DHE	dihydroethidium
DMT-1	divalent metal transporter 1
ETC	electron transport chain
FPN	ferroportin
GPX	glutathione peroxidase
GR	glutathione reductase
GSH	reduced glutathione
GSSG	oxidized glutathione
HELP	Human Explanted Heart Program
HF-MID	heart failure with myocardial iron deficiency
HF-NID	heart failure without myocardial iron deficiency
HOPE	Human Organ Procurement and Exchange Program
LVIDd/LVIDs	LV internal dimensions at end-diastole/end-systole
MDA	Malondialdehyde
MID	myocardial iron deficiency
NFC	Non-failing control

benefits constituting a promising therapeutic target.^{2,4,10} However, the diagnosis of SID is solely relied on circulating hematopoietic markers, and screening for SID in patients with HF without anemia remains uncommon. Emerging evidence has highlighted the presence of myocardial iron deficiency (MID) in several HF cohorts, and consistently revealed a weak association with systemic iron status.^{11–13}

The heart has the highest metabolic demand and is fueled largely by mitochondrial activity.^{14–16} Iron is an important micronutrient whose role extends beyond oxygen transport and erythropoiesis to cellular energetics in mitochondria and oxidative stress homeostasis.¹⁷ Mechanistically, intracellular iron availability is maintained by iron trafficking pathways including uptake, utilization, storage, and excretion of the iron by cardiomyocytes.¹⁸ While systemic iron regulation is a critical determinant of erythropoiesis and anemia, homeostatic iron levels in the heart are controlled at the tissue level.^{19,20} However, the direct burden of MID in patients with HF is unknown. As such, elucidating the prevalence and mechanism of MID, and its impact on mitochondrial function and antioxidative protection directly from the human failing myocardium is clearly warranted.

Accordingly, we studied the burden of MID in the largest cohort of explanted human hearts to date and determined its pathophysiological implications on the failing hearts. Furthermore, we explored the suitability of using quantitative parametric mapping with cardiac magnetic resonance (CMR) as a non-invasive imaging modality to assess myocardial iron levels. Our results revealed a high prevalence of MID in diseased human explanted hearts which correlated with worsened clinical status and adverse remodeling. We showed greater mitochondrial damage and loss of function in the setting of MID, which was associated with overall reduced expressions of major iron importers. Magnetic resonance imaging provided a useful tool to assess myocardial iron levels, possibly guiding a precision medicine-based approach to iron supplementation therapy. Taken together, our data revealed that MID is highly prevalent in advanced HF and worsens mitochondrial function, and thereby identifying an unappreciated role for correcting MID in patients with HF.

METHODS

The data that support the findings of this study are available from the corresponding author upon reasonable request. Refer to Data S1 for expanded methods.

Human Explanted Hearts: Tissue Procurement and Preparation

Heart specimens from the non-failing control (NFC, n=46) and adult failing hearts (HF, n=138) were procured from the Human Organ Procurement and Exchange (HOPE) program and Human Explanted Heart Program (HELP), respectively. Our diseased cohort consisted of patients with end-stage HF secondary to coronary artery disease (CAD, n=67) or dilated cardiomyopathy (DCM, n=71) who underwent heart transplantation. The NFC hearts were obtained from brain dead donors with no past history of major comorbidities or cardiovascular diseases, and antemortem echocardiography demonstrated normal ejection fraction of the left and right ventricles as well as normal LV dimensions.^{21–25} Informed consent was obtained from all patients and both programs conformed to the ethical principles of the Declaration of Helsinki, and were approved by the institutional review committee and Health Research Ethics Board at the University of Alberta, Edmonton, Canada. Clinical data were obtained by chart review.

Heart tissue procurement strictly followed our well-established protocols.^{21–25} Transmural myocardial samples from both ventricles were obtained by avoiding the epicardial fat and scar tissues. For this study, mid-anterior ventricular walls from both LV (approximately two-thirds below the aortic valves) and right ventricle (RV, approximately two-thirds below the tricuspid valves) were procured from the NFC and DCM failing hearts, whereas peri-infarcted and non-infarcted regions from LV were collected from failing hearts with CAD involving the left anterior descending artery (LAD). All the full-thickness specimens were snap-frozen and/or OCT-mounted frozen in liquid nitrogen, and then stored in the -80°C freezers for subsequent molecular and histochemical analyses.²⁴

Tissue Iron Level Measurement

Chamber- and pathogenesis-specific myocardial tissue iron levels were directly measured by inductively-coupled plasma resonance mass spectrometry as previously described at the Department of Pathology and Laboratory Medicine, London Health Sciences Center, and St. Joseph's Health Care, London, Western Ontario.^{26–28} Measurement of myocardial iron content was carried out from both ventricles in non-ischemic DCM and NFC hearts, while the levels from peri- and non-infarction regions in LV were anatomized in relation to LAD blockade. Tissue samples were analyzed in triplicate and the average values were reported in this study.

Spectrophotometric Assays for ETC Enzymes

Supernatant from the left ventricle (LV) homogenate was used to assess the electron transport chain (ETC) enzyme activity of NADH:ubiquinone oxidoreductase (COX I), succinate dehydrogenase (SDH, COX II), decylubiquinol cytochrome c oxidoreductase (COX III), NADH cytochrome c oxidoreductase (COX I+III), succinate cytochrome c reductase (COX II+III), cytochrome c oxidase (COX IV), and citrate synthase (CS).²⁹ Enzyme activity ($\text{nmol}\cdot\text{min}^{-1}\cdot\text{mg}^{-1}$) was normalized to volume and protein concentration, following protein determination with Bradford assay. Furthermore, the reaction specificity was assured by subtracting the inhibitor-resistant activity from the total enzymatic activity, which were conducted in parallel. The inhibitor for COX I (1mM rotenone), COX II (1 M malonate), COX III (1 mg/mL antimycin A), COX I+III (1 mmol/L rotenone), COX II+III (1 M malonate), and COX IV (10mM KCN) were added to each corresponding reaction mixture prepared separately.²⁹ Measurements were performed in triplicate.

Spectrophotometric Assays for Antioxidant Enzymes

Sample homogenates from flash-frozen LV tissues were prepared as previous described and all measurements were repeated in duplicate and the average value was used.^{26,30}

Catalase Enzyme Assay

Catalase (CAT) activity was measured according to the method described previously with minor modification.^{31,32} Specific activity (units/mg) was defined as the rate of H_2O_2 consumption per minute per milligram of protein sample.

Superoxide Dismutase Enzyme Assay

Superoxide dismutase (SOD) activity was assayed based on the competition for O_2^- between (ferri-)cytochrome c and SOD following its spontaneous dismutation with minor modifications.^{31,33} One unit of activity was defined as the amount of SOD required to inhibit the initial reduction rate of ferri-cytochrome c by 50%. Mitochondrial SOD (SOD2, Mn/Fe-SOD) activity was determined by adding 100 mmol/L KCN to a matched reaction mixture prepared from the same sample. The overall Cu/Zn-SOD activities from cytosol (SOD1) and extracellular matrix (SOD3) were completely inhibited by the KCN (100 mmol/L) added.³⁴

Glutathione Peroxidase Enzyme Assay

Glutathione peroxidase (GPX) activity was measured based on the oxidation of reduced glutathione

(GSH) by GPX coupled to the disappearance of NADPH catalyzed by glutathione reductase (GR).^{31,34} The rate of NADPH oxidation was monitored spectrophotometrically at 340 nm. Briefly, 2 assays (A & B) were prepared each containing 0.1 M K₂HPO₄/1 mmol/L EDTA (pH 7.0), 10 mmol/L L-glutathione reduced (G4251, Sigma, MO), 2.4 unit/

mL glutathione reductase (G3664, Sigma, MO). The non-enzymatic and H₂O₂-independent NADPH depletion were subtracted from the total GPX activity, by comparing the absorbance changes after addition of H₂O₂ in the assays. Activities were normalized to the added lysate volume and protein concentration.

Table 1. Baseline Clinical Characteristics of Patients With Normal Myocardial Iron Levels Versus Myocardial Iron Deficiency

	HF-NID (N=106)	HF-MID (N=32)	P value
Clinical			
Age, y	54.5 (47.0–61.75)	54.5 (41.8–60.3)	0.904
Sex, Male	92 (87)	24 (75)	0.110
Pathogenesis, DCM	53 (50)	18 (56)	0.535
BMI, kg/m ²	26.3 (24.2–30.2)	27.7 (24.6–30.6)	0.631
Physical assessment			
SBP, mm Hg	100.0 (88.0–120.0)	100.0 (90.0–115.0)	0.865
DBP, mm Hg	64.0 (56.0–72.0)	63.0 (51.5–73.0)	0.535
Electrocardiography			
QRS duration, ms	122.0 (92.0–151.0)	136.0 (104.8–164.0)	0.180
AF	19 (18)	8 (24)	0.377
LBBB	12 (11)	3 (10)	0.757
Echocardiography			
LA volume index, mL/m ²	43.5 (32.6–61.9)	47.3 (30.0–57.8)	0.944
LVPWT, mm	8.9 (8.0–10.0)	8.5 (8.2–10.0)	0.952
RVSP, mm Hg	35.8 (26.6–47.9)	34.1 (28.2–37.2)	0.298
TAPSE, mm	1.4 (1.0–1.8)	1.4 (1.1–1.8)	0.952
RVd Basal, cm	4.2 (3.6–4.9)	4.2 (3.9–4.8)	0.484
Blood parameters			
Ferritin, µg/L	142.5 (61.3–309.0)	91.0 (47.0–151.0)	0.103
Serum iron, µmol/L	10.0 (8.5–13.0)	10.5 (6.3–14.0)	0.667
TIBC, µmol/L	54.0 (47.0–63.0)	61.0 (53.3–72.0)	0.093
sTF (%)	19.5 (13.8–27.3)	17.0 (9.3–19.8)	0.150
Hemoglobin, g/L	128.5 (111.0–140.0)	125.5 (108.5–135.3)	0.424
MCV, fL	90.0 (86.0–95.0)	89.5 (86.8–92.3)	0.757
MCHC, g/L	336.0 (330.0–342.0)	332.5 (322.5–338.5)	0.067
eGFR, mL/min per 1.73 m ²	55.0 (41.0–70.0)	58.5 (47.0–76.8)	0.384
Devices			
Pacemaker	65 (61)	21 (66)	0.660
ICD/BiV-ICD	86 (81)	27 (84)	0.676
VAD	67 (63)	20 (63)	0.942
Medications			
ACEi/ARB	81 (76)	28 (88)	0.177

ACEi indicates angiotensin converting enzyme inhibitors; AF, atrial fibrillation; ARB, angiotensin receptor blockers; BiV-ICD, bi-ventricular implantable cardioverter-defibrillator; BMI, body mass index; DBP, diastolic blood pressure; DCM, dilated cardiomyopathy; eGFR, estimated glomerular filtration rate based on MDRD equation; LBBB, left bundle-branch block; LVPWT, left ventricular posterior wall thickness; MCHC, mean corpuscular hemoglobin concentration; MCV, mean corpuscular volume; NYHA, New York Heart Association Functional Classification; RVd Basal, basal right ventricular diameter; RVSP, right ventricular systolic pressure; SBP, systolic blood pressure; sTF, saturation of transferrin; TAPSE, tricuspid annular plane systolic excursion; and TIBC, total iron binding capacity. Categorical variables reported by count with percentage in parenthesis: sex, pathogenesis, diagnosis of AF and LBBB, device implantation, and medications. Continuous variables reported by median with interquartile range in parenthesis: age, BMI, physical assessment, QRS duration, echocardiography, and blood parameters.

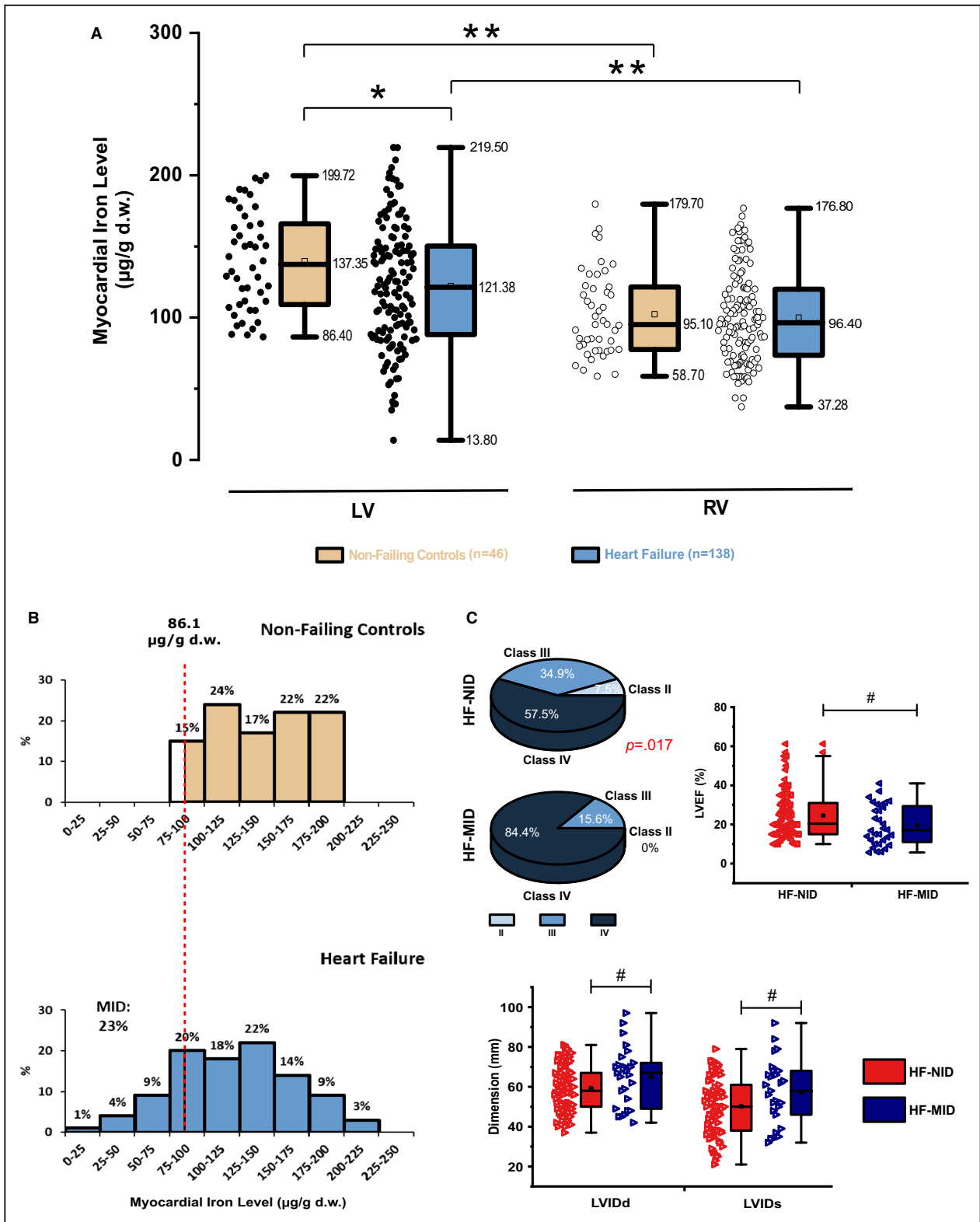
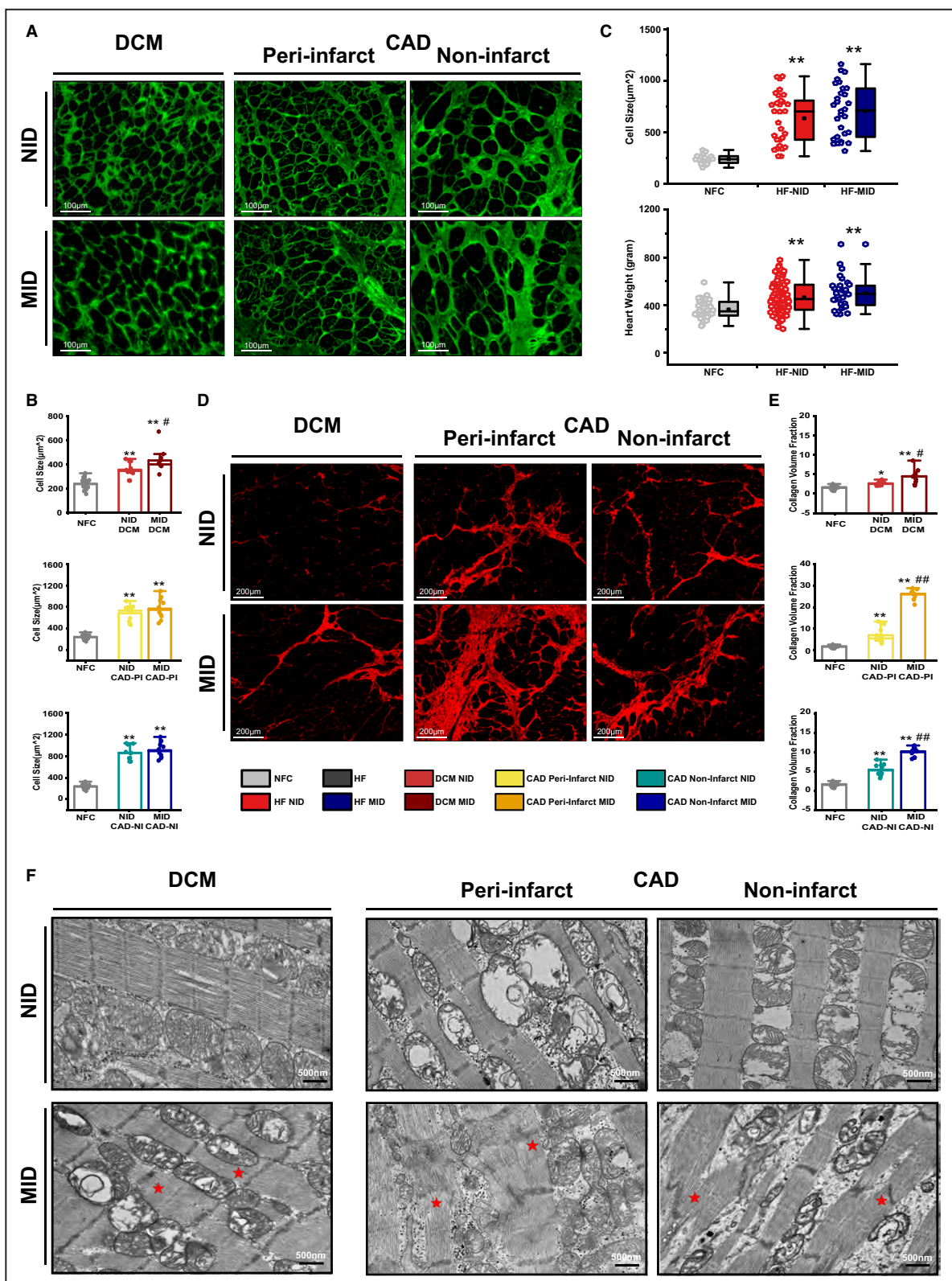


Figure 1. Myocardial iron deficiency in failing explanted human hearts with chamber-specific features of iron levels. **A**, Myocardial iron levels in the left (LV) and right ventricles (RV) in non-failing control (NFC, n=46) and explanted failing hearts (HF, n=138). **B**, Distribution of myocardial iron levels and the definition of myocardial iron deficiency (MID) with a cutoff value of 86.1 µg/g dry weight separating out 23% of patients with HF. **C**, NYHA classification, LVEF, LVIDs and LVIDd in HF-NID (n=106) versus HF-MID (n=32). HF-MID indicates patients with HF with myocardial iron deficiency; HF-NID indicates patients with HF without myocardial iron deficiency; LVEF, LV ejection fraction; LVIDd, LV end-diastolic internal diameter; LVIDs, LV end-systolic internal diameter; and NYHA, New York Heart Association. *P<0.05, **P<0.01 compared with NFC; #P<0.05, ##P<0.01 compared with HF-NID.



Measurement of Myocardial Oxidative Stress Malondialdehyde Assay

Myocardial malondialdehyde (MDA) levels were assayed using a commercially available colorimetric kit

in accordance with the manufacturer's instructions (Abcam, ab233471). The total concentration of free MDA (µmol/L per mg) was determined by reference to the MDA standard curve correcting for the sample lysate dilution as well as total amount of protein

Figure 2. Adverse myocardial remodeling in failing hearts is exacerbated by myocardial iron deficiency.

A through **C**, Representative wheat germ agglutinin staining (scale bar=100 μ m) (**A**), cardiomyocyte cross-sectional area across diseased subgroups (n=20 for NFC, n=10 for each HF subgroup) (**B**), and heart weight (n=46 for NFC; n=106 for HF-NID and n=32 HF-MID groups) (**C**) showing greater hypertrophy in the explanted failed hearts compared with non-failing controls (NFC). **D** and **E**, Representative picrosirius red staining (**D**) and relative quantification (**E**) of myocardial fibrillar content exhibiting significantly higher fibrosis in the iron-deficient failing hearts. n=20 for NFC, n=10 for each HF subgroup. **F**, Representative TEM images illustrating myofilament disarray, derangement and lysis in the HF subgroups identified from both DCM and CAD samples (scale bar=500 nm; asterisks represent areas with severe alterations). CAD-NI indicates non-infarcted from coronary artery disease; CAD-PI, peri-infarcted from coronary artery disease; DCM, dilated cardiomyopathy; MID, myocardial iron deficiency; NFC, non-failing controls; NID, no myocardial iron deficiency; and TEM, transmission electron microscopy. * $P<0.05$, ** $P<0.01$ compared with NFC; # $P<0.05$, ## $P<0.01$ compared with HF-NID.

loaded.^{26,35} Each sample was measured in duplicate, with the average value reported.

Glutathione Recycling Assay

Total myocardial glutathione, including the reduced (GSH), and oxidized (GSSG) forms, and their redox ratio (GSH:GSSG) were quantitated by the enzymatic recycling method with minor modification.^{27,30,36} Each sample was analyzed in triplicate, and the average value was finally adopted in our study.

Dihydroethidium Staining and Densitometry

In situ generation of reactive oxygen species (ROS) was determined by incubating the 5–10 μ m cryosections with dihydroethidium dye (DHE, D1168, Invitrogen), following the application of TrueBlack Lipofuscin Quencher (#23007, Biotium). The superoxide, as the redox indicator, was fluorescently visualized red within nucleus under Olympus IX81 fluorescence microscope. Quantitative measurements of DHE fluorescence intensity, corrected by the average pixel intensity from the background, were further carried out using MetaMorph software (Basic version, 7.7.0.0, Molecular Devices, Inc.).^{26,35,37–39}

Subcellular Fractionation and Western Blot

Subcellular fractionations were carried out as previously described with modifications.⁴⁰ The purity of each fraction was further validated by using anti-rabbit TLR-4 (Santa Cruz, sc-10741; membrane marker), anti-rabbit Caspase-3 (Cell Signaling, 9662S; cytosolic marker), and anti-rabbit Histone H3 (Cell Signaling, 4499s; nuclear marker).⁴¹ Western blot was performed on flash snap-frozen human myocardium tissues as we previously published.^{40,41} The below primary antibodies were used: anti-rabbit TFR-1 (Cell Signaling, 13208s); anti-rabbit FPN (Novus, NBP1-21502); anti-rabbit FTN (Abcam, ab75973); anti-mouse DMT-1 (Abcam, ab55735), followed by incubation with HRP-conjugated secondary antibodies at 1/5000 dilution (Cell Signaling). The total protein loadings were visualized by MemCode reversible stain (24585, Thermo Scientific) as a loading

control. Fiji ImageJ software (NIH, Bethesda, MD) was used for band intensity quantitation.

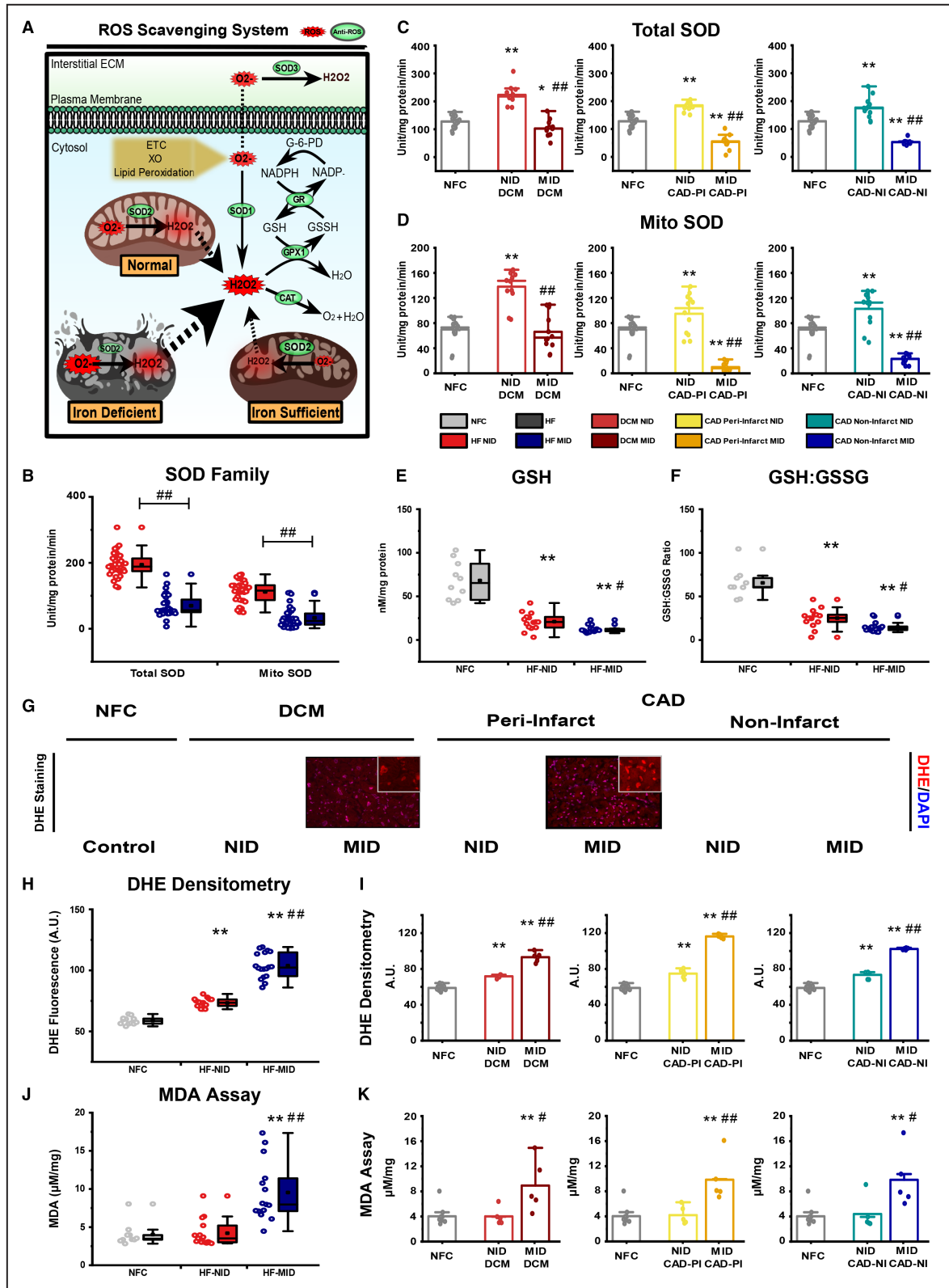
Histological Analysis and Confocal Microscopy

The 5 μ m thick sections of the formalin-fixed paraffin-embedded tissue were stained with picrosirius red (PSR) and Masson's trichrome stain for morphometric analyses as described previously.^{26,27} From each heart, n=2 sections were stained with n=20–25 random images analyzed from each section in a blinded manner. Cardiomyocyte cross-sectional area was evaluated as using fluorescence wheat-germ agglutinin staining previously published.^{21,26,40} From each heart, n=2 sections (including one technical control) were examined, with n=20–25 random images captured from each section in a blinded manner. Within each image, n=25 cardiomyocytes were unbiasedly sampled from whole regions (4 corners and center) into our analyses.

Non-specific autofluorescences (mainly lipofuscin) from the human OCT-embedded blocks were eliminated by applying TrueBlack Lipofuscin Quencher (#23007, Biotium) to the cryosections, followed by standardized tissue fixation, deparaffinization, antigen retrieval and permeabilization. The sections were then incubated with primary antibodies overnight as per manufacturer instructions, followed by incubation with fluorochrome conjugated secondary antibodies (Invitrogen). Intracellular protein colocalizations were acquired under laser scanning confocal microscopy (Leica TCS SP5, Leica Microsystems), and quantitative analyses were performed using Fiji ImageJ software.⁴⁰

Transmission Electron Microscopy

Fresh transmural myocardium from LV (<1 mm³) were promptly fixed in 2% glutaraldehyde upon explantation. The post-fixative samples were immersed in solution of 2% uranyl acetate (UA) and 0.1 M sodium acetate (pH 5.2) for high-contrast *en bloc* staining, followed by dehydration using graded ethanol and acetone solutions, and immediate infiltration with Spurr resin (Leica Electron Microscopy Sciences, Hatfield, PA). Two resin blocks per sample were sectioned



along the longitudinal axis of myofilaments to produce 4 non-consecutive ultrathin sections (70 μm), which were further post-stained with 4% UA and 4% lead citrate.

Four 100 μm^2 regions were randomly selected to obtain n=1 image at 2000 \times , n=4 images at 4000 \times , and n=6 images at 10000 \times resolutions per section for a total of 44 images per sample (H7650, Hitachi,

Figure 3. Greater oxidative stress in iron deficient failing explanted hearts.

A, Schematic of the mitochondrial function and role of iron in enzymes involved in oxidative stress. **B** through **D** Superoxide dismutase (SOD) activity assays showing overall reduced myocardial antioxidant capacity based on total (**B, C**) and mitochondrial (**B, D**) SOD activities. $n=20$ for NFC; $n=12$ for each HF subgroup with $n=36$ for HF-MID and HF-NID, respectively. **E** and **F**, Reduced glutathione (GSH, **E**) and reduced/oxidized glutathione (GSH/GSSG, **F**) ratio in HF samples further exacerbated in the MID group. $n=10$ NFC; $n=18$ each for HF-NID and HF-MID groups. **G** through **I** Representative dihydroethidium-stained images (**G**) and corresponding densitometries (**H, I**) delineating the markedly elevated oxidative stress (reflected as the total superoxide levels) in the failing human hearts, which was further inflamed by myocardial iron insufficiency. $n=12$ for NFC; $n=6$ for each HF subgroup with $n=18$ for HF-MID and HF-NID, respectively. Scale bar=100 μm . **J** and **K** Quantitative colorimetry of the total free malondialdehyde levels highlighting the aggravated lipid peroxidation in iron-deficient failing myocardium (**J**), which could consistently be alleviated by restoring iron levels in patients with HF with DCM or CAD (**K**). $n=10$ for NFC; $n=5$ for each HF subgroup with $n=15$ for either HF-MID or HF-NID. CAD-NI indicates non-infarcted from coronary artery disease; CAD-PI, peri-infarcted from coronary artery disease; DCM, dilated cardiomyopathy; MID, myocardial iron deficiency; and NID, no myocardial iron deficiency. * $P<0.05$, ** $P<0.01$ compared with NFC; # $P<0.05$, ## $P<0.01$ compared with HF-NID.

Tokyo, Japan). We established a scoring system evaluating the presence and severity of intramitochondrial inclusions, mitochondrial cristae quality as well as sarcomeric integrity, in which a higher score signified a greater severity of dysfunction (Table S1). Blinded assessment of all images was randomly carried out in triplicate by 2 examiners, and a third adjudicator was involved should any discrepancies arise between the grading.

CMR Imaging

Frozen myocardium from the middle of interventricular septum were adopted to evaluate the tissue iron content by CMR mappings. Based on LV iron level, $n=10$ and $n=4$ samples were retrospectively included in the NFC group and each HF subgroup, respectively. However, the subsequent sample preparation, image acquisition, and analytical processing were conducted in a double-blinded manner. Possible interferences from specimen dimension, environment temperature or surrounding buffer heterogeneity were eliminated by strictly following same sample preparation.⁴²

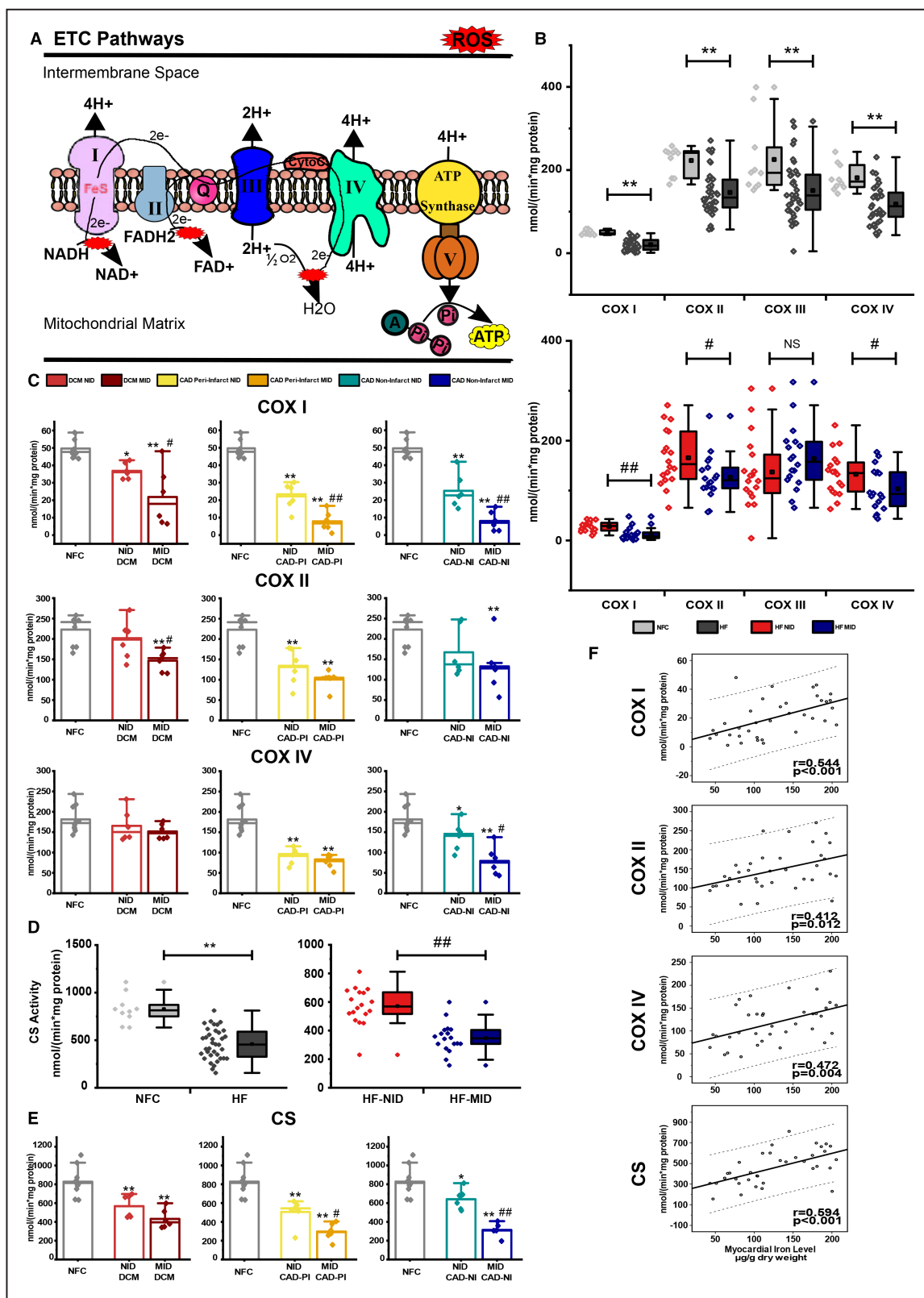
CMR experiments were performed on a 3T MRI scanner (MAGNETOM Prisma; Siemens Healthcare; Erlangen, Germany) with body coil excitation and a 2.5 cm surface coil for signal reception. Longitudinal relaxation time (T_1) images were acquired with a saturation-recovery gradient-echo pulse sequence with the following parameters: 10 slices (no gap), 1 mm slice thickness, 30 mm by 60 mm field of view, 128 phase-encoding, and 256 readout points for 0.23 mm in-plane spatial resolution. Saturation-recovery images with a recovery time of $TS=1000$ ms and full recovery were used to calculate T_1 in each pixel. Transverse relaxation time (T_2) images were acquired with a spin-echo sequence with identical spatial coverage and resolution as the T_1 acquisition, with echo-times of $TE=11$ ms in steps of 11 ms to 88 ms. T_2^* images were acquired with a multi-echo gradient-echo sequence with identical spatial coverage and resolution as the T_1 and T_2 acquisitions.

Averaged relaxation values (measured in msec) from all pixels within each tissue sample were automatically selected for analyses; all measurements were completed in duplicate.

Statistical Analysis

The normality of data distribution and homogeneity of variance were firstly assessed by Shapiro-Wilk test and Levene test, respectively. Continuous variables were presented as medians with interquartile ranges (median, Q1–Q3) for clinical parameters, or means \pm standard deviations (mean \pm SD) for experimental measurements. Categorical data were summarized as numbers with percentages (integer, %). One-way ANOVA (followed by Tukey post hoc analysis), or independent sample t -test was used to compare continuous variables between groups, while Mann-Whitney U test or Kruskal Wallis test was applied for non-parametric comparisons as appropriate. All categorical data were analyzed by Chi-squared test or Fisher's exact test where applicable. Continuous data sets were visualized by box plots with overlapping data points, or bar charts (upper line of the bar represents mean value) in a consistent manner. Pearson's correlation or Spearman rank correlation was used to evaluate the statistical association between variables of interest, including parametric and non-parametric variates, respectively. Multiple linear regression models were performed to estimate the relationship between 2 or more explanatory variables and the dependent variable, including the logistic regression algorithm for binary outcome prediction.

Briefly, multiple linear regression model was performed (Table S2) to explore the estimated coefficients of multiparametric CMR (including T_1 , T_2 , and T_2^*) and HF pathogenesis in predicting myocardial iron content. In this model, the myocardial iron level was the outcome variable, whereas the 3 CMR mapping sequences (measured in msec) and one etiological category (1: non-failing control; 2: heart failure) were the predictor



variables. The “Enter” method (direct entry) was accepted for the variable selection in this linear regression model. Data visualization and graphical representation was performed on Origin for Windows, Version

2018b (OriginLab Corp., M.A.). IBM SPSS Statistics for Windows, Version 21 (IBM Corp., N.Y.) was used for data analysis and narrative interpretation. A two-tailed *P* value <0.05 was considered statistically significant.

Figure 4. Assessment of electron transport chain pathway and the impact of myocardial iron deficiency.

A. Schematic of the electron transport chain (ETC) for ATP production and its role in the generation of reactive oxygen species (ROS). **B and C,** Reduction in enzymatic activities of complex I, II, III, and IV in HF samples (top panel) with greater functional decrease seen in complex I, II and IV in HF-MID (bottom panel) (**B**), which were further stratified based on pathogenesis (**C**). A greater reduction in complex I and II activities were observed in DCM and CAD samples with MID, while reduced complex IV activity was restricted to iron-deficient samples with CAD. $n=10$ for NFC, $n=36$ for HF; $n=6$ for each HF subgroup with $n=18$ for HF-MID and HF-NID, respectively. **D and E,** Decreased citrate synthase (CS) activity in HF samples (left panel) compared to NFC, and it was exacerbated in HF samples with MID (right panel) (**D**), which was primarily driven by lowered CS activity in the iron-depleted peri-infarct and non-infarct regions from CAD (**E**). $n=10$ for NFC, $n=36$ for HF; $n=6$ for each HF subgroup with $n=18$ for HF-MID and HF-NID, respectively. **F,** Linear regression analyses showing the strong dependence of complex I, II, IV, and CS enzyme activities on myocardial iron levels within HF cohort. $n=36$ for each enzyme, and dotted lines represent 95% CI. CAD-NI indicates non-infarcted from coronary artery disease; CAD-PI, peri-infarcted from coronary artery disease; COX I-IV, complexes I-IV; DCM, dilated cardiomyopathy; MID, myocardial iron deficiency; and NID, no myocardial iron deficiency. * $P<0.05$, ** $P<0.01$ compared with NFC; # $P<0.05$, ## $P<0.01$ compared with HF-NID.

RESULTS

Prevalence of Myocardial Iron Deficiency and Its Association With Clinical Characteristics in Patients With End-Stage Heart Failure

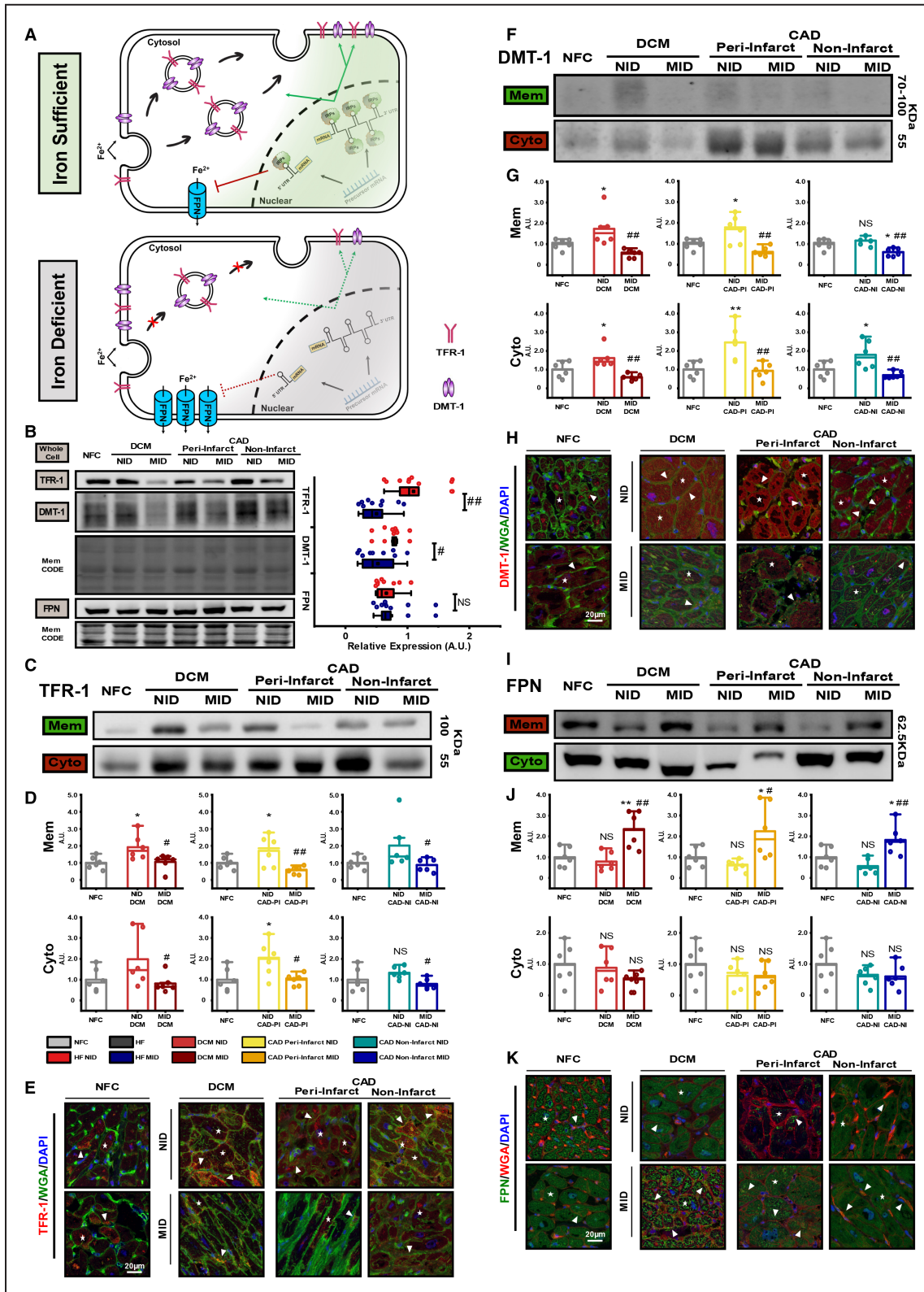
We examined the chamber-specific myocardial iron levels in explanted human hearts which included a total of 46 non-failing donor hearts and 138 failing hearts with a primary pathogenesis of DCM ($n=71$) or CAD ($n=67$) (Table; Table S3). The LV had higher myocardial iron content than the RV in both NFC [LV: 137.4 (109.2–165.9) versus RV: 95.1 (77.6–121.5) $\mu\text{g/g}$ dry weight, $P<0.001$] and HF [LV: 121.4 (88.1–150.3) compared with RV: 96.40 (73.5–120.0) $\mu\text{g/g}$ d.w., $P<0.001$] groups (Figure 1A). Surprisingly, iron level decreased only in the LV of patients with HF ($P=0.015$) with similar changes seen between the 2 etiological cohorts, while no difference was observed in the RV between NFC and HF groups ($P=0.648$) indicating MID is a major insult to the systemic ventricle (Figure 1A). Accordingly, we defined MID with a priori threshold <86.1 $\mu\text{g/g}$ d.w. in LV, based on its distinct distribution pattern between non-diseased and failing hearts (Figure 1B). Our tissue-based approach clearly separated NFC from the HF cohort resulting in $n=32$ (23%) failing hearts classified as iron-deficient for the first time (Figure 1B). Our analyses also revealed that MID is LV-specific and subsequent molecular investigations were all performed using LV samples.

Our NFC group consisted of 46 donors (male: 50%), with a median age of 47.0 years (28.0–56.5), heart weight of 350.0 grams (312.0–427.0), and LV ejection fraction (LVEF) of 60% (52.5%–62.5%) in the absence of major comorbidities and cardiovascular diseases. The HF-MID had comparable demographics, comorbid and cardiovascular history, hemodynamic parameters, and medical therapy as the patients with HF with normal myocardial iron levels (HF-NID, Table 1). We found no correlations between myocardial iron content and hemoglobin ($r=0.017$, $P=0.84$), serum ferritin ($r=0.028$, $P=0.82$), and systemic iron levels ($r=0.173$, $P=0.23$) in

the HF cohorts indicating that in the absence of distinct systemic iron deficiency (SID) and severe anemia, MID is a highly localized to the heart (Figure S1). Importantly, HF-MID patients had remarkably higher NYHA class (II/III/IV, HF-MID: 0/15.6/84.4 versus HF-NID: 7.5/34.9/57.5%, $P=0.017$), and worsened myocardial remodeling and systolic function as reflected by greater lowering in LVEF (HF-MID: 17.1 [11.5–29.1] versus HF-NID: 20.4 [15.0–31.3]%, $P=0.04$) and larger increase in LV internal dimensions at end-systole (LVIDs, HF-MID: 58.0 [47.0–67.0] versus HF-NID: 50.0 [38.3–60.8] mm, $P=0.03$) and end-diastole (LVIDd, HF-MID: 67.0 [51.5–71.5] versus HF-NID: 58.0 [50.3–67.0] mm, $P=0.03$) (Figure 1C).

Myocardial Iron Deficiency Is Linked to Adverse Myocardial Remodeling and Mitochondrial Dysfunction

We next examined the cellular and subcellular characteristics of the explanted failing hearts (LV) to correlate the effects of MID on adverse myocardial remodeling. Increased myocardial hypertrophy and interstitial fibrosis are prominent features of heart diseases.^{43,44} Cardiomyocyte size assessed by WGA staining displayed greater increase in the failed hearts regardless of cardiac iron status compared with NFC (NFC: 239.6 ± 46.4 versus HF: 670.0 ± 248.6 μm^2 , $P<0.001$), which was consistent with our gravimetric analysis of the explanted hearts (NFC: 363.0 ± 74.3 versus HF: 472.4 ± 130.0 gram, $P<0.001$) (Figure 2A through 2C; Figure S2A). Meanwhile, PSR staining captured strikingly higher fibrosis in the failing hearts which was further exacerbated in the HF-MID group (Figure 2D and 2E; Figure S2B), and it was confirmed by classic Masson's trichrome staining (Figure S2C). Next, we developed a comprehensive scoring system evaluating cardiomyocyte ultrastructure, presence and severity of intramitochondrial inclusions and mitochondrial cristae quality (Table S1). Myofilament disarray and severe lysis were identified in the HF-MID group in both DCM and CAD samples, in comparison with NFC (Figure 2F; Figure S2D and S2E). Qualitative assessment of the



mitochondria using TEM showed severe distortion of cristae and increased inclusion bodies in the HF-MID group with occasional mitochondrial lysis (Figure S3). These features demonstrated exacerbation of the

adverse remodeling in the explanted failing human hearts with MID. A central role of iron relates to the superoxide dismutase (SOD) family which provides a key defense

Figure 5. Assessment of iron transporters using immunoblotting analysis and immunofluorescence staining with confocal microscopy.

A, Schematic of the key iron transporters and the role of the iron regulatory proteins in a cardiomyocyte. **B**, Immunoblotting analysis (left panel) and quantification (right panel) of the total transferrin receptor 1 (TFR-1), divalent metal transporter 1 (DMT-1), and ferroportin (FPN) levels showing overall decreased TFR-1 and DMT-1 expressions in HF-MID, after normalized to NFCs. $n=3$ for each HF subgroup with $n=9$ for HF-MID and HF-NID, respectively. **C** through **E**, Subcellular immunoblotting analysis with representative bands (**C**) and quantification (**D**) of TFR-1 showing overall reduced expressions in both membrane and cytosolic fractions in samples with MID, which was confirmed by immunofluorescence staining (**E**). **F** through **H**, Similarly, subcellular immunoblotting analysis with representative bands (**F**) and quantification (**G**) of DMT-1 showing overall reduced expressions in both membrane and cytosolic fractions in HF subgroups with MID, which was supported by immunofluorescence staining (**H**). **I** through **K**, Subcellular western blot analysis (**I**) and quantification (**J**) of FPN, and immunofluorescence staining (**K**) showing its relative increase in membrane fraction but not in cytosol in samples with MID. CAD-NI indicates non-infarcted from coronary artery disease; CAD-PI, peri-infarcted from coronary artery disease; Cyto, cytosol; DAPI, 4',6-diamidino-2-phenylindole; DCM, dilated cardiomyopathy; Mem, membrane; MID, myocardial iron deficiency; NID, no myocardial iron deficiency; and WGA, wheat germ agglutinin. Arrowheads indicated membrane colocalization while asterisks refer to the cytosolic location of the proteins. $n=10$ for NFC; $n=6$ each for HF subgroups for all subcellular immunoblotting analyses. * $P<0.05$, ** $P<0.01$ compared with NFC; # $P<0.05$, ## $P<0.01$ compared with HF-NID.

against superoxide radicals (O_2^-) produced in the mitochondria as a byproduct of the respiratory chain activity (Figure 3A). We assessed total SOD and mitochondria-specific (SOD2) enzymatic activities. While the enzymatic activities of total (NFC: 127.4 ± 22.1 versus HF: 131.8 ± 71.2 unit/mg protein per min, $P=0.786$) and mitochondrial (NFC: 69.9 ± 16.8 versus HF: 72.5 ± 50.8 unit/mg protein per min, $P=0.822$) isoforms were comparable between the 2 groups, we further identified a marked suppression of their ROS-scavenging capacities in the HF-MID group (Figure 3B), with concordant changes seen across all etiological subgroups (Figure 3C and 3D). In contrast, functional activities of 2 downstream antioxidant enzymes, catalase (CAT) and glutathione peroxidase-1 (GPX1), were not affected by myocardial iron levels (Figure S4A and S4B). Overall, myocardial reduced glutathione (GSH) levels and GSH to oxidized glutathione (GSSG) ratio were further decreased in iron-deficient failing hearts (Figure 3E and 3F) likely due to the loss of SOD-related antioxidant protections.^{26,34} While markedly elevated oxidative stress within failing myocardium was delineated by DHE staining, the corresponding densitometric analyses confirmed higher level of superoxide associated with myocardial iron insufficiency across all subgroups (Figure 3G through 3I). Additionally, we observed aggravated lipid peroxidation profiles specifically in iron-deficient failing hearts, consistent with increased oxidative damage in these hearts (Figure 3J and 3K).

Iron is a component of iron-sulfur (Fe-S) clusters in the electron transport chain (ETC) pathways, which in combination with increased oxidative stress and ultrastructural abnormalities, implicates dysfunctional respiratory and metabolic activities in the mitochondria (Figure 4A). Complex-specific activity assays showed a selective loss of complex I, II, IV (Figure 4B and 4C), and citrate synthase (CS, Figure 4D and 4E) activities in HF-MID with no decline in complex III functional activity (Figure S4C). Moreover, the enzyme activities of ETC complex I ($r=0.54$, $P<0.001$), II ($r=0.41$, $P=0.012$), and IV ($r=0.47$, $P=0.004$) and CS ($r=0.59$, $P<0.001$) within the

citric acid cycle correlated positively with myocardial iron levels in failing hearts, providing further evidence for a direct relationship between myocardial iron status and mitochondrial enzyme activities (Figure 4F). These results demonstrated that lowered myocardial iron in human hearts was closely associated with unfavorable myocardium remodeling, and could further exacerbate oxidative stress and deplete respiratory chain activity in the setting of advanced HF.

Role of Iron Trafficking System in Myocardial Iron Deficiency

Myocardial iron homeostasis is orchestrated by a tightly controlled regulatory system involving transcriptional control of the iron regulatory protein (IRP-1/-2) axis and corresponding changes in key iron transporters, namely transferrin receptor-1 (TFR-1), divalent metal transporter-1 (DMT-1), and ferroportin (FPN) (Figure 5A).^{17,19} We showed that total levels of TFR-1 and DMT-1 were reduced in HF-MID compared with iron-sufficient failing hearts by 54.3% and 31.4%, respectively, while the overall level of FPN remained unchanged between 2 groups (Figure 5B; Figure S5). Next, we investigated the intracellular translocation of iron transporters between cytosolic and plasma membrane compartments respectively (Figure 5C through 5K), following our validated subcellular fractionation protocol (Figure S6A and Figure S6B). Likewise, our immunoblotting analysis of major iron importers demonstrated that HF-MID had significantly reduced membrane and cytosolic levels of both TFR-1 (Figure S6C, Figure S7) and DMT-1 (Figure S6D, Figure S8) when compared with their iron-sufficient counterparts. Interestingly, there was relatively increased expression of FPN on sarcolemma without noticeable change seen in the cytosolic fraction (Figure S6E, Figure S9) of iron-deficient failing myocardium. The subcellular distribution and shift of iron transporters was further examined across all HF subgroups (Figure 5C through 5K) and similar findings of TFR-1 (Figure 5C and 5D; Figure S7),

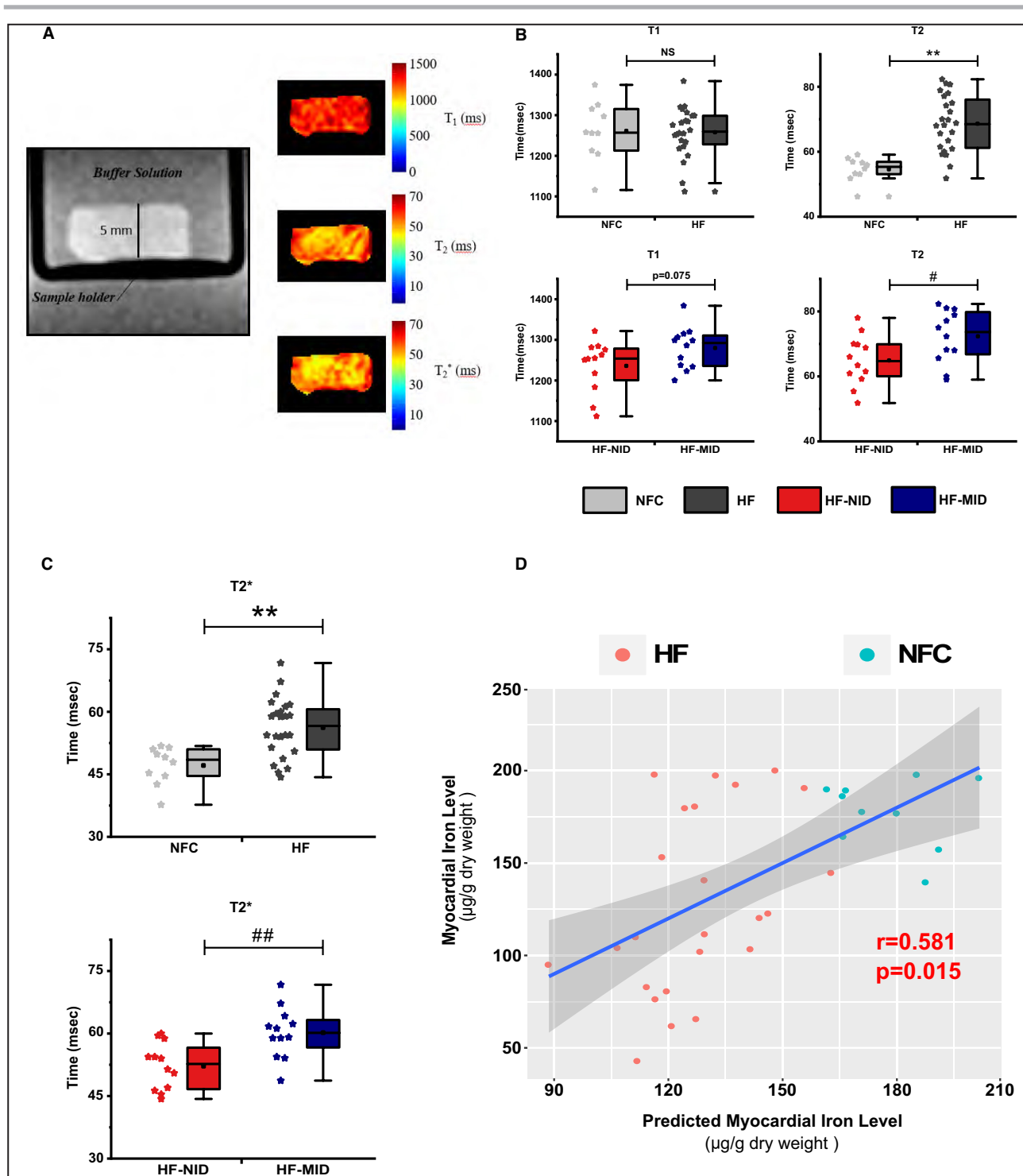


Figure 6. Magnetic resonance imaging of explanted human heart samples in relation to myocardial iron levels.

A through **C**, Typical parametric maps (T_1 , T_2 and T_2^*) from a representative sample are illustrated (**A**) allowing for the quantitative assessment using T_1 and T_2 (**B**) and T_2^* values (**C**) in non-failing controls (NFC) and HF subgroups consist of DCM and CAD. **D**, Multiple linear regression analysis using T_1 , T_2 , T_2^* and pathogenesis as covariates showing a moderately strong relationship with myocardial iron levels ($r=0.581$; $P=0.015$; $n=34$). NID=no iron deficiency; MID=myocardial iron deficiency. $n=10$ for NFC, $n=24$ for HF; $n=4$ for each HF subgroup with $n=12$ for HF-MID and HF-NID, respectively. * $P<0.05$, ** $P<0.01$ compared with NFC; # $P<0.05$, ## $P<0.01$ compared with HF-NID.

DMT-1 (Figure 5F and 5G; Figure S8), and FPN (Figure 5I and 5J; Figure S9) were observed in DCM and CAD samples with MID, indicating that restricted iron uptake with concomitant iron efflux can underlie the basis of MID in failing hearts. We next used immunofluorescent staining of the iron transporters in DCM and CAD samples to confirm the subcellular location and concordance of changes seen in the Western blot analysis (Figure 5E, 5H, 5K; Figure S10). Collectively, our results demonstrated a differential subcellular regulation of iron transporters in MID characterized by reduced membrane and cytosolic levels of iron uptake transporters, TFR-1 and DMT1, and increased levels of the iron exporter, FPN, in the membrane.

Myocardial Iron Levels Assessed by CMR Imaging

In the absence of overt SID, we evaluated quantitative imaging using CMR relaxation time constants as a non-invasive assessment of myocardial iron status. In our study, we explored the feasibility of applying T1, T2, and T2* evaluations in tissue samples using CMR technique (Figure 6A). Our analyses showed that significantly elevated T2 (Figure 6B) and T2* values (Figure 6C) were featured in iron-deficient failing hearts, with similar changes seen between healthy control and diseased groups. However, T1 signal did not exhibit such distinct alteration (Figure 6B). Multivariate analysis incorporating T1, T2, T2*, and pathogenesis showed moderate predictability of myocardial iron levels providing a reliable and non-invasive methodology to determine myocardial iron levels (Figure 6D; Table S2). These results demonstrated the ability of CMR to detect and accurately reflect myocardial iron levels as a promising clinical surrogate in patients with advanced HF.

DISCUSSION

Elucidating and treating comorbidities in patients with HF remains a pivotal approach to minimize morbidity and mortality. While systemic iron deficiency and anemia in acute and patients with chronic HF are associated with worsened clinical outcome, iron supplementation in these patients improved prognosis.^{3,7,45–47} Current guidelines for the diagnosis and treatment of HF clearly endorse a class I recommendation of iron deficiency and anemia screening in all patients.^{2,4} Given that the dominant mechanism of iron regulation occur at the tissue level, myocardial iron homeostasis can be uncoupled from systemic iron profile.^{8,45,48} However, the primary determinant of the myocardial iron levels in failing human hearts remains unexplored. Our prospective human explanted heart program has provided a valuable resource with extensive collection

of explanted human heart specimens and clinical phenotypes, thereby facilitating the examination of myocardial iron regulation in relation to advanced HF.^{24,25} We performed the largest translational study examining myocardial iron levels directly from the LV and RV of explanted human hearts in patients with DCM or CAD.

Our results established that MID in advanced failing hearts is associated with greater adverse remodeling including interstitial fibrosis and cardiac hypertrophy, as well as worsened LVEF and NYHA classification. Interestingly, myocardial iron levels in RV were coherently lower compared with LV regardless of pathogenesis, and the lack of MID in the RV indicated divergent adverse remodelling progression in those patients with HF.⁴⁹ We also showed that LV-specific MID was associated with further suppressed ROS-scavenging capacity, excessive oxidative stress, and impaired mitochondrial respiratory function and altered ultrastructure integrity. While our results were correlative in nature, they were consistent with prior studies directly linking iron deficiency to impaired human cardiomyocyte function and mitochondrial respiration.^{15,50} Human embryonic stem cell-derived cardiomyocytes depleted of iron affected mitochondrial function through reduced activity of the Fe-S cluster-containing complexes I, II and III with reduced ATP levels and contractile force.¹⁵ Fe-S clusters are ubiquitous cofactors composed of iron and inorganic sulfur, which are required for the proper function of Fe-S proteins involved in a wide range of biological activities, including electron transport in respiratory chain, micronutrient (i.e., iron) sensing, DNA repair and a key component of antioxidant enzymes.

The steady-state level of myocardial iron is maintained by the concerted action of major iron importers, TRF-1 and DMT-1, and the sole iron exporter, FPN.^{17,20,51–53} The expressions of TRF-1 and DMT-1 are positively regulated by the nuclear transcriptional factors, IRP-1 and IRP-2, and cardiac selective disruption in the IRP-1/2 axis led to MID and cardiac dysfunction.^{19,20} Surprisingly, there was reduced membrane translocation of TRF-1 and DMT-1 likely a result of the defective IRP-1/2 pathway in HF-MID, which clearly was inadequate to restore myocardial iron status. Disruption in IRP-1/2 action would conversely lead to increased translation of FPN mRNA. Indeed, we observed relatively increased membrane fractions of FPN facilitating iron efflux from the failing cardiomyocytes, which is supported by findings in a genetic murine model.⁵² Suppression of FPN in the membrane compartment provides a promising foundation for correcting MID in patients with advanced HF.

The exact mechanisms by which patients with HF develop MID are not completely understood. An interplay between increased sympathetic activation and iron deficiency was recently observed in patients with chronic HF, suggesting the latter could be more

than a comorbidity but a critical component leading to HF.⁵⁴ Our data supported the hypothesis that iron deficiency is an integral pathophysiology promoting the progression to advanced HF, and that low iron storage in patients with HF is independently associated with escalated rates of mortality and re-hospitalizations.⁵⁵ In addition, our results were consistent with clinical trial findings showing that the treatment of iron deficiency irrespective of anemia was beneficial.⁴⁷ Regulation of skeletal muscle energetics also represents an important mechanism by which iron supply confers benefits in HF in addition to its central role in myocardial iron homeostasis.⁵⁶

Different therapeutic possibilities embrace iron replacement by oral or IV routes. Several clinical trials with IV iron in chronic patients with HF with SID, have demonstrated equally efficacious and similar favorable safety profiles following correction of iron levels, irrespective of anemia.^{10,56} Thus, iron status should be assessed in symptomatic patients with HF both with or without anemia, and treatment of iron deficiency warrants consideration in clinical practice.⁴⁷ The use of CMR to diagnose myocardial iron-overload is a valid and established technique.⁵⁷ Our ability to extend the evaluation of myocardial iron levels using CMR to iron-deficient hearts provides a unique tool to potentially diagnose and monitor patients with HF with MID. Our findings illustrate the potential for precision medicine and correction of MID, especially given the widespread clinical availability of parametric mapping with CMR and its assessment of myocardial iron levels.^{42,57–59} Animal models with selective MID and cardiac dysfunction are corrected by the IV administration of iron supporting the distinct possibility of this approach in patients.²⁰ In patients with heart failure and iron deficiency, IV ferric carboxymaltose administration changed T2* and T1 cardiac MRI parameters indicative of myocardial iron repletion, further supporting the utility of cardiac MRI to monitor myocardial iron deficiency and its response to therapy.⁵⁹

There are a few limitations of our study that need to be acknowledged. First, our investigation was cross-sectional and all patients included were at end-stage HF, and thus we captured a single time point of the entire disease course thereby limiting the ascertainment of causative relationship when interpreting the experimental results. Secondly, while our non-failing control hearts demonstrated no evidence of adverse remodeling characteristic of heart failure, they do not represent the true normal myocardium in vivo for reasons including, but not limited to, antemortem medications and metabolic alteration in relation to initial injuries, and postmortem adrenergic storm associated with brain death. In order to minimize these limitations, we used a large number of samples coupled with a comprehensive profile of clinical parameters including

comorbidities, past medical history, and treatments, which were integrated into specimen assessment, subgrouping, and data interpretation.

ARTICLE INFORMATION

Received December 13, 2021; accepted April 14, 2022.

Affiliations

Division of Cardiology, Department of Medicine (H.Z., A.N., Z.T., F.W., G.Y.O.), Department of Pharmacology (K.L.J., J.M.S.), Department of Biomedical Engineering (J.G., R.T.), Division of Cardiac Surgery, Department of Surgery (S.W.), Faculty of Medicine and Dentistry, University of Alberta, Edmonton, Alberta, Canada; Mazankowski Alberta Heart Institute (H.Z., J.G., A.N., Z.T., F.W., S.W., R.T., J.M.S., G.Y.O.); Now with Yale University School of Medicine, New Haven, CT (Z.T.); Department of Genetics, Harvard Medical School (J.G.S., C.E.S.); and Cardiovascular Division, Brigham and Women's Hospital, Boston, MA (C.E.S.).

Acknowledgments

We would like to acknowledge the support we received from our altruistic donors and their families.

Sources of Funding

This work was supported by the Canadian Institutes of Health Research [CIHR, PJ 44352] and Heart & Stroke Foundation [177654] to GYO. This work was supported, in part, by CIHR project grant [FRN 156393] to JMS. HZ is supported by the China Scholarship Council (CSC) Award.

Disclosures

None.

Supplemental Material

Data S1
Tables S1–S3
Figures S1–S10

REFERENCES

- Virani SS, Alonso A, Benjamin EJ, Bittencourt MS, Callaway CW, Carson AP, Chamberlain AM, Chang AR, Cheng S, Delling FN, et al. American Heart Association Council on Epidemiology and Prevention Statistics Committee and Stroke Statistics Subcommittee. Heart disease and stroke statistics-2020 update: a report from the American Heart Association. *Circulation*. 2020;141:e139–e596. doi: [10.1161/CIR.0000000000000757](https://doi.org/10.1161/CIR.0000000000000757)
- Yancy CW, Jessup M, Bozkurt B, Butler J, Casey DE, Colvin MM, Drazner MH, Filippatos GS, Fonarow GC, Givertz MM, et al. 2017 ACC/AHA/HFSA focused update of the 2013 ACCF/AHA guideline for the management of heart failure: a report of the American College of Cardiology/American Heart Association Task Force on Clinical Practice Guidelines and the Heart Failure Society of America. *Circulation*. 2017;136:e137–e161. doi: [10.1161/CIR.0000000000000509](https://doi.org/10.1161/CIR.0000000000000509)
- Anand IS, Gupta P. Anemia and Iron deficiency in heart failure: current concepts and emerging therapies. *Circulation*. 2018;138:80–98. doi: [10.1161/CIRCULATIONAHA.118.030099](https://doi.org/10.1161/CIRCULATIONAHA.118.030099)
- Ponikowski P, Voors AA, Anker SD, Bueno H, Cleland JGF, Coats AJS, Falk V, González-Juanatey JR, Harjola V-P, Jankowska EA, et al. 2016 ESC guidelines for the diagnosis and treatment of acute and chronic heart failure: the task force for the diagnosis and treatment of acute and chronic heart failure of the European Society of Cardiology (ESC) developed with the special contribution of the Heart Failure Association (HFA) of the ESC. *Eur Heart J*. 2016;37:2129–2200. doi: [10.1093/eurheartj/ehw128](https://doi.org/10.1093/eurheartj/ehw128)
- Klip IT, Comin-Colet J, Voors AA, Ponikowski P, Enjuanes C, Banasiak W, Lok DJ, Rosentryt P, Torrens A, Polonski L, et al. Iron deficiency in chronic heart failure: an international pooled analysis. *Am Heart J*. 2013;165:575–582.e3. doi: [10.1016/j.ahj.2013.01.017](https://doi.org/10.1016/j.ahj.2013.01.017)
- Tkaczyszyn M, Comin-Colet J, Voors AA, van Veldhuisen DJ, Enjuanes C, Moliner-Borja P, Rozentryt P, Poloński L, Banasiak W, Ponikowski P,

- et al. Iron deficiency and red cell indices in patients with heart failure. *Eur J Heart Fail.* 2018;20:114–122. doi: [10.1002/ejhf.820](https://doi.org/10.1002/ejhf.820)
7. Jankowska EA, Malyszko J, Ardehali H, Koc-Zorawska E, Banasiak W, von Haehling S, Macdougall IC, Weiss G, McMurray JJV, Anker SD, et al. Iron status in patients with chronic heart failure. *Eur Heart J.* 2013;34:827–834. doi: [10.1093/eurheartj/ehs377](https://doi.org/10.1093/eurheartj/ehs377)
 8. Jankowska EA, von Haehling S, Anker SD, Macdougall IC, Ponikowski P. Iron deficiency and heart failure: diagnostic dilemmas and therapeutic perspectives. *Eur Heart J.* 2013;34:816–829. doi: [10.1093/eurheartj/ehs224](https://doi.org/10.1093/eurheartj/ehs224)
 9. Okonko DO, Mandal AK, Missouri CG, Poole-Wilson PA. Disordered iron homeostasis in chronic heart failure: prevalence, predictors, and relation to anemia, exercise capacity, and survival. *J Am Coll Cardiol.* 2011;58:1241–1251. doi: [10.1016/j.jacc.2011.04.040](https://doi.org/10.1016/j.jacc.2011.04.040)
 10. Anker SD, Comin Colet J, Filippatos G, Willenheimer R, Dickstein K, Drexler H, Lüscher TF, Bart B, Banasiak W, Niewowska J, et al. Ferric carboxymaltose in patients with heart failure and iron deficiency. *N Engl J Med.* 2009;361:2436–2448. doi: [10.1056/NEJMoa0908355](https://doi.org/10.1056/NEJMoa0908355)
 11. Maeder MT, Khammy O, dos Remedios C, Kaye DM. Myocardial and systemic iron depletion in heart failure implications for anemia accompanying heart failure. *J Am Coll Cardiol.* 2011;58:474–480. doi: [10.1016/j.jacc.2011.01.059](https://doi.org/10.1016/j.jacc.2011.01.059)
 12. Leszek P, Sochanowicz B, Szperl M, Kolsut P, Brzóska K, Piotrowski W, Ryzwik TM, Danko B, Polkowska-Motrenko H, Rózański JM, et al. Myocardial iron homeostasis in advanced chronic heart failure patients. *Int J Cardiol.* 2012;159:47–52. doi: [10.1016/j.ijcard.2011.08.006](https://doi.org/10.1016/j.ijcard.2011.08.006)
 13. Melenovsky V, Petrak J, Mracek T, Benes J, Borlaug BA, Nuskova H, Pluhacek T, Spatenka J, Kovalcikova J, Drahota Z, et al. Myocardial iron content and mitochondrial function in human heart failure: a direct tissue analysis. *Eur J Heart Fail.* 2017;19:522–530. doi: [10.1002/ejhf.640](https://doi.org/10.1002/ejhf.640)
 14. Neubauer S. The failing heart—An engine out of fuel. *N Engl J Med.* 2007;356:1140–1151. doi: [10.1056/NEJMra063052](https://doi.org/10.1056/NEJMra063052)
 15. Hoes MF, Grote Beverborg N, Kijlstra JD, Kuipers J, Swinkels DW, Giepmans BNG, Rodenburg RJ, van Veldhuisen DJ, de Boer RA, van der Meer P. Iron deficiency impairs contractility of human cardiomyocytes through decreased mitochondrial function. *Eur J Heart Fail.* 2018;20:910–919. doi: [10.1002/ejhf.1154](https://doi.org/10.1002/ejhf.1154)
 16. van der Meer P, van der Wal HH, Melenovsky V. Mitochondrial function, skeletal muscle metabolism, and iron deficiency in heart failure. *Circulation.* 2019;139:2399–2402. doi: [10.1161/CIRCULATIONAHA.119.040134](https://doi.org/10.1161/CIRCULATIONAHA.119.040134)
 17. Zhang H, Zhabyeyev P, Wang S, Oudit GY. Role of iron metabolism in heart failure: from iron deficiency to iron overload. *Biochim Biophys Acta Mol Basis Dis.* 2019;1865:1925–1937. doi: [10.1016/j.bbdis.2018.08.030](https://doi.org/10.1016/j.bbdis.2018.08.030)
 18. Galy B, Ferring-Appel D, Sauer SW, Kaden S, Lyoumi S, Puy H, Kolker S, Grone HJ, Hentze MW. Iron regulatory proteins secure mitochondrial iron sufficiency and function. *Cell Metab.* 2010;12:194–201. doi: [10.1016/j.cmet.2010.06.007](https://doi.org/10.1016/j.cmet.2010.06.007)
 19. Zhabyeyev P, Oudit GY. Unravelling the molecular basis for cardiac iron metabolism and deficiency in heart failure. *Eur Heart J.* 2017;38:373–375.
 20. Haddad S, Wang Y, Galy B, Korf-Klingebiel M, Hirsch V, Baru AM, Rostami F, Rebol MR, Heineke J, Flogel U, et al. Iron-regulatory proteins secure iron availability in cardiomyocytes to prevent heart failure. *Eur Heart J.* 2017;38:362–372. doi: [10.1093/eurheartj/ehw333](https://doi.org/10.1093/eurheartj/ehw333)
 21. Jana S, Zhang H, Lopaschuk GD, Freed DH, Sergi C, Kantor PF, Oudit GY, Kassiri Z. Disparate remodeling of the extracellular matrix and proteoglycans in failing pediatric versus adult hearts. *J Am Heart Assoc.* 2018;7:e010427. doi: [10.1161/JAHA.118.010427](https://doi.org/10.1161/JAHA.118.010427)
 22. Chen X, Zhabyeyev P, Azad AK, Wang W, Minerath RA, DesAulniers J, Grueter CE, Murray AG, Kassiri Z, Vanhaesebroeck B, et al. Endothelial and cardiomyocyte PI3K β divergently regulate cardiac remodeling in response to ischaemic injury. *Cardiovasc Res.* 2019;115:1343–1356. doi: [10.1093/cvr/cvr298](https://doi.org/10.1093/cvr/cvr298)
 23. Chen X, Zhabyeyev P, Azad AK, Vanhaesebroeck B, Grueter CE, Murray AG, Kassiri Z, Oudit GY. Pharmacological and cell-specific genetic PI3K α inhibition worsens cardiac remodeling after myocardial infarction. *J Mol Cell Cardiol.* 2021;157:17–30. doi: [10.1016/j.yjmcc.2021.04.004](https://doi.org/10.1016/j.yjmcc.2021.04.004)
 24. Zhang H, Viveiros A, Nikhanj A, Nguyen Q, Wang K, Wang W, Freed DH, Mullen JC, MacArthur R, Kim DH, et al. The human explanted heart program: a translational bridge for cardiovascular medicine. *Biochimica Et Biophysica Acta (BBA) - Molecular Basis of Disease.* 2021;1867:165995–166009. doi: [10.1016/j.bbdis.2020.165995](https://doi.org/10.1016/j.bbdis.2020.165995)
 25. Litviňuková M, Talavera-López C, Maatz H, Reichart D, Worth CL, Lindberg EL, Kanda M, Polanski K, Heinig M, Lee M, et al. Cells of the adult human heart. *Nature.* 2020;588:466–472. doi: [10.1038/s41586-020-2797-4](https://doi.org/10.1038/s41586-020-2797-4)
 26. Das SK, Wang W, Zhabyeyev P, Basu R, McLean B, Fan D, Parajuli N, DesAulniers J, Patel VB, Hajjar RJ, et al. Iron-overload injury and cardiomyopathy in acquired and genetic models is attenuated by resveratrol therapy. *Sci Rep.* 2015;5:18132. doi: [10.1038/srep18132](https://doi.org/10.1038/srep18132)
 27. Oudit GY, Trivieri MG, Khaper N, Husain T, Wilson GJ, Liu P, Sole MJ, Backx PH. Taurine supplementation reduces oxidative stress and improves cardiovascular function in an iron-overload murine model. *Circulation.* 2004;109:1877–1885. doi: [10.1161/01.CIR.0000124229.40424.80](https://doi.org/10.1161/01.CIR.0000124229.40424.80)
 28. Oudit GY, Sun H, Trivieri MG, Koch SE, Dawood F, Ackerley C, Yazdanpanah M, Wilson GJ, Schwartz A, Liu PP, et al. L-type Ca²⁺ channels provide a major pathway for iron entry into cardiomyocytes in iron-overload cardiomyopathy. *Nat Med.* 2003;9:1187–1194. doi: [10.1038/nm920](https://doi.org/10.1038/nm920)
 29. Spinazzi M, Casarin A, Pertegato V, Salviati L, Angelini C. Assessment of mitochondrial respiratory chain enzymatic activities on tissues and cultured cells. *Nat Protoc.* 2012;7:1235–1246. doi: [10.1038/nprot.2012.058](https://doi.org/10.1038/nprot.2012.058)
 30. Das SK, Patel VB, Basu R, Wang W, DesAulniers J, Kassiri Z, Oudit GY. Females are protected from iron-overload cardiomyopathy independent of iron metabolism: key role of oxidative stress. *J Am Heart Assoc.* 2017;6. doi: [10.1161/JAHA.116.003456](https://doi.org/10.1161/JAHA.116.003456)
 31. Weydert CJ, Cullen JJ. Measurement of superoxide dismutase, catalase and glutathione peroxidase in cultured cells and tissue. *Nat Protoc.* 2010;5:51–66. doi: [10.1038/nprot.2009.197](https://doi.org/10.1038/nprot.2009.197)
 32. Zhang Y, El-Sikhry H, Chaudhary KR, Batchu SN, Shayeganpour A, Jukar TO, Bradbury JA, Graves JP, DeGraff LM, Myers P, et al. Overexpression of CYP2J2 provides protection against doxorubicin-induced cardiotoxicity. *Am J Physiol Heart Circ Physiol.* 2009;297:H37–H46. doi: [10.1152/ajpheart.00983.2008](https://doi.org/10.1152/ajpheart.00983.2008)
 33. Jamieson KL, Keshavarz-Bahaghghat H, Darwesh AM, Sosnowski DK, Seubert JM. Age and sex differences in hearts of soluble epoxide hydrolase null mice. *Front Physiol.* 2020;11:48. doi: [10.3389/fphys.2020.00048](https://doi.org/10.3389/fphys.2020.00048)
 34. Dieterich S, Bielick U, Beulich K, Hasenfuss G, Prestle J. Gene expression of antioxidative enzymes in the human heart: increased expression of catalase in the end-stage failing heart. *Circulation.* 2000;101:33–39. doi: [10.1161/01.CIR.101.1.33](https://doi.org/10.1161/01.CIR.101.1.33)
 35. Patel VB, Wang Z, Fan D, Zhabyeyev P, Basu R, Das SK, Wang W, Desaulniers J, Holland SM, Kassiri Z, et al. Loss of p47phox subunit enhances susceptibility to biomechanical stress and heart failure because of dysregulation of cortactin and actin filaments. *Circ Res.* 2013;112:1542–1556. doi: [10.1161/CIRCRESAHA.111.300299](https://doi.org/10.1161/CIRCRESAHA.111.300299)
 36. Rahman I, Kode A, Biswas SK. Assay for quantitative determination of glutathione and glutathione disulfide levels using enzymatic recycling method. *Nat Protoc.* 2006;1:3159–3165. doi: [10.1038/nprot.2006.378](https://doi.org/10.1038/nprot.2006.378)
 37. Patel VB, Bodiga S, Basu R, Das SK, Wang W, Wang Z, Lo J, Grant MB, Zhong JC, Kassiri Z, et al. Loss of angiotensin-converting enzyme-2 exacerbates diabetic cardiovascular complications and leads to systolic and vascular dysfunction: a critical role of the angiotensin II/AT1 receptor axis. *Circ Res.* 2012;110:1322–1335. doi: [10.1161/CIRCRESAHA.112.268029](https://doi.org/10.1161/CIRCRESAHA.112.268029)
 38. Bodiga S, Zhong JC, Wang W, Basu R, Lo J, Liu GC, Guo D, Holland SM, Scholey JW, Penninger JM, et al. Enhanced susceptibility to biomechanical stress in ACE2 null mice is prevented by loss of the p47(phox) NADPH oxidase subunit. *Cardiovasc Res.* 2011;91:151–161. doi: [10.1093/cvr/cvr036](https://doi.org/10.1093/cvr/cvr036)
 39. Zhong J, Basu R, Guo D, Chow FL, Byrns S, Schuster M, Loibner H, Wang X-H, Penninger JM, Kassiri Z. Angiotensin-converting enzyme 2 suppresses pathological hypertrophy, myocardial fibrosis, and cardiac dysfunction. *Circulation.* 2010;122:717–728, 18 p following 728. doi: [10.1161/CIRCULATIONAHA.110.955369](https://doi.org/10.1161/CIRCULATIONAHA.110.955369)
 40. Patel VB, Zhabyeyev P, Chen X, Wang F, Paul M, Fan D, McLean BA, Basu R, Zhang P, Shah S, et al. PI3K α -regulated gelsolin activity is a critical determinant of cardiac cytoskeletal remodeling and heart disease. *Nat Commun.* 2018;9:5390.
 41. Wang W, McKinnie SMK, Patel VB, Haddad G, Wang Z, Zhabyeyev P, Das SK, Basu R, McLean B, Kandalam V, et al. Loss of Apelin exacerbates myocardial infarction adverse remodeling and ischemia-reperfusion injury: therapeutic potential of synthetic Apelin analogues. *J Am Heart Assoc.* 2013;2:e000249. doi: [10.1161/JAHA.113.000249](https://doi.org/10.1161/JAHA.113.000249)

42. Messroghli DR, Moon JC, Ferreira VM, Grosse-Wortmann L, He T, Kellman P, Mascherbauer J, Nezafat R, Salerno M, Schelbert EB, et al. Clinical recommendations for cardiovascular magnetic resonance mapping of T1, T2, T2* and extracellular volume: a consensus statement by the Society for Cardiovascular Magnetic Resonance (SCMR) endorsed by the European Association for Cardiovascular Imaging (EACVI). *J Cardiovasc Magn Reson*. 2017;19:75. doi: [10.1186/s12968-017-0389-8](https://doi.org/10.1186/s12968-017-0389-8)
43. Burchfield JS, Xie M, Hill JA. Pathological ventricular remodeling: mechanisms: part 1 of 2. *Circulation*. 2013;128:388–400. doi: [10.1161/CIRCULATIONAHA.113.001878](https://doi.org/10.1161/CIRCULATIONAHA.113.001878)
44. Kim GH, Uriel N, Burkhoff D. Reverse remodelling and myocardial recovery in heart failure. *Nat Rev Cardiol*. 2018;15:83. doi: [10.1038/nrcardio.2017.139](https://doi.org/10.1038/nrcardio.2017.139)
45. Jankowska EA, Kasztura M, Sokolski M, Bronisz M, Nawrocka S, Olekowska-Florek W, Zymliński R, Biegus J, Siwoowski P, Banasiak W, et al. Iron deficiency defined as depleted iron stores accompanied by unmet cellular iron requirements identifies patients at the highest risk of death after an episode of acute heart failure. *Eur Heart J*. 2014;35:2468–2476. doi: [10.1093/eurheartj/ehu235](https://doi.org/10.1093/eurheartj/ehu235)
46. van Deursen VM, Urso R, Laroche C, Damman K, Dahlstrom U, Tavazzi L, Maggioni AP, Voors AA. Co-morbidities in patients with heart failure: an analysis of the European Heart Failure Pilot Survey. *Eur J Heart Fail*. 2014;16:103–111. doi: [10.1002/ejhf.30](https://doi.org/10.1002/ejhf.30)
47. Filippatos G, Farmakis D, Colet JC, Dickstein K, Lüscher TF, Willenheimer R, Parissis J, Gaudesius G, Mori C, von Eisenhart Rothe B, et al. Intravenous ferric carboxymaltose in iron-deficient chronic heart failure patients with and without anaemia: a subanalysis of the FAIR-HF trial. *Eur J Heart Fail*. 2013;15:1267–1276. doi: [10.1093/eurjhf/hft099](https://doi.org/10.1093/eurjhf/hft099)
48. Wish JB. Assessing iron status: beyond serum ferritin and transferrin saturation. *Clin J Am Soc Nephrol*. 2006;1:S4–S8. doi: [10.2215/CJN.01490506](https://doi.org/10.2215/CJN.01490506)
49. Reddy S, Bernstein D. Molecular mechanisms of right ventricular failure. *Circulation*. 2015;132:1734–1742. doi: [10.1161/CIRCULATIONAHA.114.012975](https://doi.org/10.1161/CIRCULATIONAHA.114.012975)
50. Kobak KA, Radwanska M, Dziegala M, Kasztura M, Josiak K, Banasiak W, Ponikowski P, Jankowska EA. Structural and functional abnormalities in iron-depleted heart. *Heart Fail Rev*. 2019;24:269–277. doi: [10.1007/s10741-018-9738-4](https://doi.org/10.1007/s10741-018-9738-4)
51. Xu W, Barrientos T, Mao L, Rockman HA, Sauve AA, Andrews NC. Lethal cardiomyopathy in mice lacking transferrin receptor in the heart. *Cell Rep*. 2015;13:533–545. doi: [10.1016/j.celrep.2015.09.023](https://doi.org/10.1016/j.celrep.2015.09.023)
52. Lakhal-Littleton S, Wolna M, Carr CA, Miller JJJ, Christian HC, Ball V, Santos A, Diaz R, Biggs D, Stillion R, et al. Cardiac ferroportin regulates cellular iron homeostasis and is important for cardiac function. *Proc Natl Acad Sci USA*. 2015;112:3164–3169. doi: [10.1073/pnas.1422373112](https://doi.org/10.1073/pnas.1422373112)
53. Lakhal-Littleton S, Wolna M, Chung YJ, Christian HC, Heather LC, Brescia M, Ball V, Diaz R, Santos A, Biggs D, et al. An essential cell-autonomous role for hepcidin in cardiac iron homeostasis. *Elife*. 2016;5. doi: [10.7554/eLife.19804](https://doi.org/10.7554/eLife.19804)
54. Moliner P, Enjuanes C, Tajés M, Cainzos-Achirica M, Lupón J, Garay A, Jimenez-Marrero S, Yun S, Farré N, Cladellas M, et al. Association between norepinephrine levels and abnormal iron status in patients with chronic heart failure: is iron deficiency more than a comorbidity? *J Am Heart Assoc*. 2019;8:e010887. doi: [10.1161/JAHA.118.010887](https://doi.org/10.1161/JAHA.118.010887)
55. Grote Beverborg N, van der Wal HH, Klip IT, Anker SD, Cleland J, Dickstein K, van Veldhuisen DJ, Voors AA, van der Meer P. Differences in clinical profile and outcomes of low iron storage vs defective iron utilization in patients with heart failure: results from the DEFINE-HF and BIostat-CHF studies. *JAMA Cardiol*. 2019;4:696–701. doi: [10.1001/jamacardio.2019.1739](https://doi.org/10.1001/jamacardio.2019.1739)
56. Charles-Edwards G, Amaral N, Sleigh A, Ayis S, Catibog N, McDonagh T, Monaghan M, Amin-Youssef G, Kemp GJ, Shah AM, et al. Effect of iron isomaltoside on skeletal muscle energetics in patients with chronic heart failure and iron deficiency. *Circulation*. 2019;139:2386–2398. doi: [10.1161/CIRCULATIONAHA.118.038516](https://doi.org/10.1161/CIRCULATIONAHA.118.038516)
57. Carpenter J-P, He T, Kirk P, Roughton M, Anderson LJ, de Noronha SV, Sheppard MN, Porter JB, Walker JM, Wood JC, et al. On T2* magnetic resonance and cardiac iron. *Circulation*. 2011;123:1519–1528. doi: [10.1161/CIRCULATIONAHA.110.007641](https://doi.org/10.1161/CIRCULATIONAHA.110.007641)
58. Lota AS, Gatehouse PD, Mohiaddin RH. T2 mapping and T2* imaging in heart failure. *Heart Fail Rev*. 2017;22:431–440. doi: [10.1007/s10741-017-9616-5](https://doi.org/10.1007/s10741-017-9616-5)
59. Núñez J, Miñana G, Cardells I, Palau P, Liàcer P, Fàcila L, Almenar L, López-Lereu MP, Monmeneu JV, Amiguet M, et al. Noninvasive imaging estimation of myocardial iron repletion following administration of intravenous iron: the Myocardial-IRON trial. *J Am Heart Assoc*. 2020;9:e014254. doi: [10.1161/JAHA.119.014254](https://doi.org/10.1161/JAHA.119.014254)

SUPPLEMENTAL MATERIAL

Data S1. Supplemental Methods

Spectrophotometric Assays for ETC Enzymes

Ground tissues from the left ventricle (LV) were homogenized in ice-cold homogenization buffer (20mM Tris, 40mM KCl, 2mM EGTA, pH=7.4, with 50mM sucrose added day of homogenization). Samples were centrifuged at 600g for 10 minutes at 4°C to remove cellular debris. Supernatant was collected and used to assess the electron transport chain (ETC) enzyme activity of NADH:ubiquinone oxidoreductase (COX I), succinate dehydrogenase (SDH, COX II), decylubiquinol cytochrome c oxidoreductase (COX III), NADH cytochrome c oxidoreductase (COX I + III), succinate cytochrome c reductase (COX II + III), cytochrome c oxidase (COX IV) and citrate synthase (CS).²⁹ Enzyme activity ($\text{nmol}\cdot\text{min}^{-1}\cdot\text{mg}^{-1}$) was normalized to volume and protein concentration, following protein determination with Bradford assay. Specifically, it is calculated based on the following equation: enzyme activity = $\frac{\Delta\text{Absorbance}/\text{min} \times 1000}{[(\text{extinction coefficient} \times \text{volume of sample loaded in ml}) \times (\text{protein concentration of sample in mg/ml})]}$. Furthermore, the reaction specificity was assured by subtracting the inhibitor-resistant activity from the total enzymatic activity, which were conducted in parallel. The inhibitor for COX I (1mM rotenone), COX II (1M malonate), COX III (1mg/ml antimycin A), COX I + III (1mM rotenone), COX II + III (1M malonate), and COX IV (10mM KCN) were added to each corresponding reaction mixture prepared separately.²⁹ Measurements were performed in triplicate.

Spectrophotometric Assays for Antioxidant Enzymes

As described previously, flash-frozen LV tissues were homogenized by using TissueLyser II ($r=25\text{rpm}$, 3min; Qiagen) and total protein were extracted in ice-cold CelLytic™ M (C2978, Sigma, MO, USA) supplemented with protease (Complete Protease Inhibitor) and phosphatase inhibitor (PhosSTOP EasyPack) (Roche, Mannheim, Germany) cocktails.^{26, 30} The homogenate was centrifuged at 14,800rpm (21,100g) for 12mins (4°C), and the enzymatic activities were examined in the aliquoted supernatants after quantitation of protein concentration using Bradford assay. All measurements were repeated in duplicate, and the average value was used.

CAT Enzyme Assay. Catalase (CAT) activity was measured according to the method described previously with minor modification.^{31, 32} Briefly, 20-40 μl tissue homogenate (100-300 μg protein) was added to 600 μl assay buffer, which contained 50mM KH_2PO_4 and 50mM Na_2HPO_4 (pH 7.0), and baseline absorbance was recorded at 240nm for 3 minutes at room temperature (RT) using a quartz cuvette. Reactions were started upon addition of 300 μl H_2O_2 (30mM) and the changes to absorbance was followed for 5 minutes. Specific activity (units/mg) was defined as the rate of H_2O_2 consumption per minute per milligram of protein sample.

SOD Enzyme Assay. Superoxide dismutase (SOD) activity was assayed based on the competition for O_2^- between (ferri-)cytochrome c and SOD following its spontaneous dismutation.^{31, 33} One unit of activity was defined as the amount of SOD required to inhibit the initial reduction rate of ferri-cytochrome c by 50%. A reaction cocktail containing 50mM $\text{KH}_2\text{PO}_4/0.1\text{mM}$ EDTA (pH 7.8), 50 μM xanthine (X0626, Sigma, MO, USA) and 10 μM cytochrome c (C2867, Sigma, MO, USA) was prepared at RT. Xanthine oxidase (6nM, X4376, Sigma, MO, USA) was added to the mixture to obtain a stable baseline reading (0.015-0.025

Abs/min) at 418 nm for 3 minutes. Reactions were started by the addition of whole cell lysate (3-15µg protein) to a quartz cuvette and absorbance was continuously monitored for 5 minutes to calculate the total SOD activities (SOD1-3). Mitochondrial SOD (SOD2, Mn/Fe-SOD) activity was determined by adding 100mM KCN to a matched reaction mixture prepared from the same sample. The overall Cu/Zn-SOD activities from cytosol (SOD1) and extracellular matrix (SOD3) are completely inhibited by the KCN (100mM) added.³⁴ The purity of cytochrome c (potential SOD contamination) was checked by adding 1mM KCN to reaction mixtures prior to the addition of any SOD-containing samples; no significant increase in cytochrome c reduction rate were noted after addition of KCN.

GPX Enzyme Assay. Glutathione peroxidase (GPX) activity was measured based on the oxidation of reduced glutathione (GSH) by GPX coupled to the disappearance of NADPH catalyzed by glutathione reductase (GR).^{31, 34} The rate of NADPH oxidation was monitored spectrophotometrically at 340nm. Briefly, two assays (A & B) were prepared each containing 0.1M K₂HPO₄/1mM EDTA (pH 7.0), 10mM L-glutathione reduced (G4251, Sigma, MO, USA), 2.4unit/ml glutathione reductase (G3664, Sigma, MO, USA). Both assays were firstly pre-incubated at 37°C for 10 minutes in the presence (assay A) and absence (assay B) of the whole cell lysate (50-150µg protein). The H₂O₂-independent NADPH oxidation in both assay reactions were monitored for 3 minutes immediately after the addition of 1.5mM NADPH (10107824001, Sigma, MO, USA). Next, pre-warmed 1mM sodium azide (catalase inhibitor; S2002, Sigma, MO, USA) and 1.5 mM H₂O₂ were added simultaneously to both assays and the reduced NADPH optical density was read every 30 seconds for 5 minutes. The non-enzymatic and H₂O₂-independent NADPH depletion were subtracted from the total GPX activity, by comparing the

absorbance changes after addition of H₂O₂ in two assays. Activities were normalized to the added lysate volume and protein concentration.

Measurement of Myocardial Lipid Peroxidation

Malondialdehyde (MDA), as an established indicator of lipid peroxidation, was measured colorimetrically using a commercial kit (Abcam, ab233471) according to the manufacturer's instructions. In detail, flash-frozen myocardium samples (~150 mg) from LV were chopped into smaller pieces and then fully homogenized using Dounce homogenizer in low pH lysis buffer (500µl/each, 20mM NaH₂PO₄ & 0.5% TritonX-100, pH 3.0-3.2) with the addition of protease (Complete Protease Inhibitor) and phosphatase (PhosSTOP EasyPack) (Roche, Mannheim, Germany) inhibitor cocktails. Following a 10-min incubation on ice, the tissue lysates were centrifuged at top speed for 6 min (13,000 rpm, 4°C) and the clear supernatants were collected or stored at -80°C for further studies. Protein concentrations were quantitated using the Bio-Rad BCA assay as aforementioned, and all the prepared reagents and materials were gently agitated after equilibrated to RT. Next, 50 µl of each sample lysate and serially diluted MDA standards (0, 6.25, 12.5, 25, 50, 100, 200, and 400 µM) were pipetted into a 96-well clear bottom microplate, immediately followed by adding 10 µl of MDA Color Reagent solution to each well and incubating at RT for 15 min in the dark. Finally, 40 µl of Reaction Solution was added to each mixture with another 45-min incubation at RT. The absorbance increases were monitored by a microplate reader (SpectraMax iD5, Molecular Devices, San Jose, CA) with path-check correction at 695 nm. The absorbance readings of blank controls (with dilution buffer or lysis buffer only) were used as the negative controls, and were subtracted from the detected values

from both the standards and experimental samples. The total concentration of free MDA ($\mu\text{M}/\text{mg}$) was determined by reference to the MDA standard curve correcting for the sample lysate dilution as well as total amount of protein loaded.^{26,35} The assay conditions (e.g., low pH) served to minimize potential interferences from other lipid peroxidation natural by-products, such as 4-hydroxyalkenals (4-HNE), and our protocol specifically probed the free MDA level within the myocardium. Each sample was assayed in duplicate, with the average value accepted.

Tissue Glutathione Level (GSH/GSSG) Measurement

Reduced (GSH), oxidized (GSSG) myocardial glutathione and their redox ratio (GSH:GSSG) were quantitated by enzymatic recycling method as described previously.^{27, 30, 36} Each sample was analyzed in triplicate, and the average value was used.

Subcellular Fractionation and Western Blot

Subcellular fractionations were performed as previously described with modifications.⁴⁰ Tissues from LV were lysed and homogenized (20 rpm/minute, 2 minutes, 4°C) in 500 μl radioimmunoprecipitation assay (RIPA, 50 mM Tris-HCl, 150mM NaCl and 1mM EDTA, pH=7.4) buffer with the addition of 1X protease inhibitor cocktail (Roche), followed by centrifugation (2900 g, 20 minutes, 4°C) to precipitate the crude nuclear from the cytosolic and membrane proteins (first supernatant). The pellet was gently washed and homogenized again using the above methods, followed by a second homogenization (25 rpm/minute, 3 minutes, 4°C) in 200 μl commercial RIPA buffer (ThermoFisher, 25mM Tris-HCl, 150mM NaCl, 1% NP-40, 1% sodium deoxycholate and 0.1% SDS) supplemented with 1X protease inhibitor cocktail

(Roche), producing pure nuclear fraction. The first supernatant was further ultra-centrifuged (29000 g, 45 minutes, 4°C) to pellet the membrane and simultaneously harvest cytosolic components from the second supernatant. The purity of each fraction was further validated by using anti-rabbit TLR-4 (Santa Cruz, sc-10741; membrane marker), anti-rabbit Caspase-3 (Cell Signaling, 9662S; cytosolic marker) and anti-rabbit Histone H3 (Cell Signaling, 4499s; nuclear marker).⁴¹

For mitochondrial fractionation, frozen LV tissues were ground and homogenized in fractionation buffer containing 250mM sucrose, 10mM Tris-HCL, 1mM EDTA, 1mM sodium orthovanadate, 1mM sodium fluoride, 10µg/L aprotinin, 2µg/L leupeptin, and 100µg/L pepstatin.³³ Homogenate was first centrifuged for 10 minutes at 700g (4°C) to remove the debris. The supernatant was decanted and centrifuged for 20 minutes at 10,000g (4°C) to obtain the “crude” mitochondrial fractions as pellet. Subsequently, the mitochondrial pellet was resuspended in fractionation buffer and protein concentrations was calorimetrically determined using the Bio-Rad BCA protein assay kit (with bovine serum albumin as standards).

Western blotting was performed on flash snap-frozen human myocardium tissues.^{40, 41} In total, 500 µg protein was extracted; and aliquots of protein (45 - 60 µg) were separated on 6% - 20% gradient sodium dodecyl sulfate polyacrylamide gel electrophoresis (SDS-PAGE) and transferred onto 0.2µm PVDF membranes. They were subject to immunoblotting with the following primary antibodies: anti-rabbit TFR-1 (Cell Signaling, 13208s); anti-rabbit FPN (Novus, NBP1-21502); anti-rabbit FTN (Abcam, ab75973); anti-mouse DMT-1 (Abcam, ab55735), and subsequently incubated with HRP-conjugated secondary antibodies at 1/5000 dilution (Cell Signaling). The protein loadings were visualized by MemCode™ reversible stain

(24585, Thermo Scientific™) of the PVDF membranes as a loading control, and all blots were scanned by ImageQuant LAS 4000 (28955810, GE Health Care, Biosciences, Uppsala, Sweden). To avoid exhausting valuable samples, some blots were reprobed with a second targeted protein after incubation in Restore™ Western Blot Stripping Buffer (ThermoFisher 21059) for 15-30 minutes (RT), followed by vigorous washing using combination of 1X TBST (3rpm, 5min x3) and 1X TBS (3rpm, 5min x3), and complete blocking by 5% non-fat milk for 1 hour (3rpm, RT). ImageJ software (NIH, USA) was used for band intensity quantitation.

Histological Analysis

The excised transmural biopsies were immediately fixed in 10% buffered formalin (containing 4% formaldehyde) followed by embedding in paraffin. Thin sections (5µm) of the tissue were stained with picro-sirius red (PSR) and Masson's trichrome stain for morphometric analysis. The tissue sections were first deparaffinized in xylene and alcohol grades, then rehydrated in water and subjected to respective staining protocols as described previously.^{26, 27} The fibrotic pattern was assessed by visualization under a bright field microscope (DM 4000 B, Leica), together with fibrillar content quantification under Olympus IX81 fluorescence microscope. Image analysis was performed on MetaMorph software (Basic version 7.7.0.0, Molecular Devices, Inc). From each heart, n=2 sections were stained with n=20-25 random images analyzed from each section in a blinded manner.

Dihydroethidium Staining and Densitometry

Dihydroethidium (DHE), a cell-permeable oxidative fluorescent probe, was applied to directly reflect the total superoxide levels from the LV specimens as previously demonstrated.^{26, 35, 37-39} Briefly, the 5-10 μm OCT-embedded cryosections were washed using Hank's Balanced Salt Solution (HBSS, #14025092, GibcoTM) with calcium chloride and magnesium chloride at RT for 5 min. A sufficient amount of (100-200 μl) TrueBlack Lipofuscin Quencher (1:20 in 70% ethanol, #23007, Biotium) was quickly applied to both experimental and control sections at RT for 5-10 min, followed by washing with HBSS (5 min/each) for another 3 times. Then, the experiment sections were incubated with DHE (1:100 in HBSS, D1168, Invitrogen) at RT for 20 min in the dark, while the negative control sections were incubated with 1X HBSS simultaneously. The sections were finally mounted using prolong gold DAPI antifade (#P36931, Invitrogen). In situ generation of superoxide was then detected qualitatively using an Olympus IX81 fluorescence microscope with multi channels (i.e., TxRed:DHE and DAPI:nuclei) selected, and the overall oxidative stress was represented as the red fluorescence intensity of the product upon oxidation – (oxy)ethidium – within the nuclei, which was readily quantifiable by MetaMorph software (Basic version, 7.7.0.0, Molecular Devices, *Inc.*). Specifically, the RGB pictures were converted into 8-bit gray scale (intensity profile: 0 to 255), and regions (n=5-10) congruent to the cell nuclei boundaries from both experimental and negative control sections were randomly drawn to calculate the average pixel intensities as the background noise. Given that all the image acquisition settings (i.e., exposure time, brightness/contrast, etc.) remained unvaried between groups, the actual oxidized DHE fluorescence was obtained by subtracting the background signal from the average pixel intensity of the nuclei using Fiji ImageJ (National

Institute of Health, Bethesda, MD, USA) software.³⁵ n=20 images/sample were blindly taken as the technical replicate with n=20-25 nuclei analyzed from each tissue section.

Immunofluorescence (IF) and Fluorescence Microscopy

Cardiomyocyte morphology was evaluated fluorescently by applying wheat germ agglutinin (WGA) staining on the optimal cutting temperature (OCT) compound-mount (TFM, General Data Company) tissue blocks, which was snap frozen in liquid nitrogen as previously published.^{21, 26, 40} Similarly, the 5-10 μm cryo-sectioned slices were fixed with 4% paraformaldehyde for 20 mins and then rehydrated in 1X PBS for 30 mins at RT. Sections were permeabilized using 100% precool methanol (-20°C) for 10mins, followed by blocking with 4% BSA for 1 hr at RT. After thorough washings, the sections were incubated with WGA (1:200, W11261, Invitrogen) for 30 mins at RT and then applied with 20 μl /section DAPI gold anti-fade mountant (#P36931, Invitrogen). The plasma membrane was fluorescently visualized under Olympus IX81 fluorescence microscope and analyzed using MetaMorph software (Basic version 7.7.0.0, Molecular Devices, Inc). From each heart, n=2 sections (including one technical control) were examined, with n=20-25 random images captured from each section in a blinded manner. Within each image, n=25 cardiomyocytes were unbiasedly sampled from whole regions (four corners & center) into our analyses.

Autofluorescence Quench and Confocal Microscopy

Non-specific autofluorescences (mainly lipofuscin) from the human OCT-embedded blocks were significantly eliminated by applying TrueBlack® Lipofuscin Quencher (#23007, Biotium)

to the cryosections for 5 mins at RT, followed by standardized tissue fixation, deparaffinization, antigen retrieval and permeabilization as described above. The sections were gently washed with 1XPBS for 3 times, blocked with 5% serum for 1 hr at RT, and incubated with primary antibody as per manufacturer instructions, namely anti-rabbit TFR-1 (Cell Signaling, 13208s), anti-rabbit FPN (Novus, NBP1-21502), and anti-mouse DMT-1 (Abcam, ab55735) overnight in a humidified hood at 4°C. Next the sections were incubated with Alexa Fluor 594-conjugated secondary antibodies (Invitrogen, USA) against the host species of individual primary antibody for 2 hrs at 37°C. Lastly the sections were stained with Alexa Fluor 488-conjugated WGA (W11261, Invitrogen) and mounted with DAPI antifade (#P36931, Invitrogen) to outline plasma membrane and nuclei, respectively. Intracellular protein colocalizations were acquired under laser scanning confocal microscopy (Leica TCS SP5, Leica Microsystems), and quantitative analyses were performed using Fiji ImageJ (National Institute of Health, Bethesda, MD, USA) software.⁴⁰

Transmission Electron Microscopy (TEM)

Human explanted myocardial specimens were collected transmurally as described above. The tissues (<1mm³) were promptly fixed in 2% glutaraldehyde with a physiological pH and 360 mOsm osmolarity at 37°C. After stored in 4°C fridges overnight, the specimens were post-fixed in 1.5% K₄Fe(CN)₆ and 2% osmium tetroxide (OsO₄) followed by complete washing with 0.1M sodium cacodylate (pH 7.2) and 0.1M sodium acetate (pH 5.2) buffers. Next, the post-fixative samples were immersed in solution of 2% uranyl acetate (UA) and 0.1M sodium acetate (pH 5.2) for high-contrast en bloc staining. Samples were dehydrated with graded ethanol and acetone

solutions, immediately followed by infiltration with Spurr's Resin (Leica Electron Microscopy Sciences, Hatfield, PA, USA). After 24 hours, two resin blocks per sample were sectioned with an ultramicrotome diamond knife along the longitudinal axis of myofilaments to produce four non-consecutive ultrathin sections (70µm), which were further post-stained with 4% UA and 4% lead citrate.

Four 100 µm² regions were randomly selected to obtain n=1 image at 2000X resolution, n=4 images at 4000X resolution, and n=6 images at 10000X resolution per sections for a total of 44 images per sample (H7650, Hitachi, Tokyo, Japan). Two investigators independently evaluated cardiomyocytes for the presence and severity of intramitochondrial inclusions, mitochondrial cristae quality as well as sarcomeric ultrastructural integrity (ImageJ software, National Institute of Health, Bethesda, MD, USA). Each mitochondrial long axis, short axis and cross-sectional surface area were measured. The cross-sectional area was defined as the region enveloped by the mitochondria outer membrane, and mitochondrial long axis was defined as the longest distance between two points on the outer membrane, while short axis was defined as the shortest distance perpendicular to the long axis. We established a scoring system in which a higher score signified a greater severity of dysfunction and based on the collective score of individual mitochondria, each heart specimen was ranked as healthy or varying degree (mild, moderate, or severe) of abnormalities (**Table S1**). For consistency, sarcomere or mitochondria whose outer membrane was cut off by the image field of view were excluded from analysis. Blinded assessment of all images was randomly carried out in triplicate by two examiners, and a third adjudicator was involved should any discrepancies arise between the individual assessments.

Cardiac Magnetic Resonance Imaging (CMR)

Frozen myocardium from the middle of interventricular septum were adopted to evaluate the tissue iron content by CMR mappings.⁴² Based on LV iron level, n=10 and n=4 samples were retrospectively included in the NFC group and each HF subgroup, respectively. However, the subsequent sample preparation, image acquisition, and analytical processing were conducted in a double-blinded manner. After rapid thawing (15 seconds) on ice, each frozen specimen was cut into cuboids with an approximate dimension of 10mm x 10mm x 5mm (length x width x thickness) with smooth edges. They were then immersed in sufficient 0.9% saline solution to gently equilibrate the tissues to RT (21°C) avoiding possible interferences from temperature,⁴² and the fresh saline solution was replaced every 10 minutes for a total of three times. To eliminate artifacts from air bubbles, the final saline buffer (50ml) was simultaneously prepared by heating the 50ml conical tube in a water bath for 30 minutes, followed by thorough sonication (FS30H, Fisher Scientific, MA, USA) for additional 30 minutes at RT. Similarly, the tapping water filling the ultrasonic bath was replaced every 10 minutes in order to equilibrate the heated buffer solution back to RT without time delay. A 10ml Pyrex[®] glass beaker (CLS100010, Aldrich, MO, USA) was assembled into the conical tube, where the prepared tissue was surrounded by homogenous deaired buffer solution and well situated at the bottom center with muscle fiber orientation in parallel to the magnetic field. All measurements were completed in duplicate.

CMR experiments were performed on a 3T MRI scanner (MAGNETOM Prisma; Siemens Healthcare; Erlangen, Germany) with body coil excitation and a 2.5 cm surface coil for signal reception. Longitudinal relaxation time (T_1) images were acquired with a saturation-

recovery gradient-echo pulse sequence with the following parameters: 10 slices (no gap), 1 mm slice thickness, 30 mm by 60 mm field of view, 128 phase-encoding and 256 readout points for 0.23 mm in-plane spatial resolution. Saturation-recovery images with a recovery time of $TS = 1000$ ms and full recovery were used to calculate T_1 in each pixel. Transverse relaxation time (T_2) images were acquired with a spin-echo sequence with identical spatial coverage and resolution as the T_1 acquisition, with echo-times of $TE=11$ ms in steps of 11 ms to 88 ms. T_2^* images were acquired with a multi-echo gradient-echo sequence with identical spatial coverage and resolution as the T_1 and T_2 acquisitions, with echo-times of $TE=3.26$ ms in steps 6.28 ms to 47.22 ms. Mono-exponential recovery was assumed for calculation of T_1 , T_2 and T_2^* (signal $(TS)=1-\exp(-TS/T_1)$ for saturation recovery imaging and $\text{signal}(TE)=\exp(-TE/T_2)$ and $\text{signal}(TE)=\exp(-TE/T_2^*)$ for T_2 and T_2^* multi-echo imaging) with pixel-by-pixel relaxation maps generated for all samples. Averaged relaxation values (measured in msec) from all pixels within each tissue sample were automatically selected for analyses; all measurements were completed in duplicate.

Table S1. Qualitative Scoring Criteria for Mitochondrial Ultrastructural Morphology and Architecture for Intra-mitochondrial Inclusion (A) and Cristae (B)

A.		Percentage of Individual Mitochondrial Inclusion Scores		
		% Mitochondria with score = 0	% Mitochondria with score = 1-2	% Mitochondria with score = 3
Overall Patient Score	Healthy	>75%	<5%	<5%
	Mild	<75%	<5%	<5%
	Moderate	<75%	>5%	<5%
	Severe	X	X	>5%

B.		Percentage of Individual Mitochondrial Cristae Scores		
		% Mitochondria with score = 0	% Mitochondria with score = 1-2	% Mitochondria with score = 3
Overall Patient Score	Healthy	>80%	<10%	<5%
	Mild	<80%	<10%	<5%
	Moderate	<80%	>10%	<5%
	Severe	X	X	>5%

Intramitochondrial inclusions score of 0 indicates no inclusions, and scores 1-3 represent the presence of mitochondrial inclusions with increasing severity. Patients with >5% mitochondria having a score of 3 are considered severe regardless of other factors. Mitochondria cristae quality score of 0 indicates healthy cristae, and scores 1-3 represent decreasing cristae quality. Patients with >5% mitochondria having a score of 3 are considered severe regardless of other factors.

Table S2. Multiple Linear Regression Model: Estimated Coefficients of CMR Mappings

Multiple Linear Regression Model	Unstandardized Coefficients		Standardized Coefficients	t	Sig.	95% Confidence Interval for B	
	B	S.E.M.	Beta			Lower Bound	Upper Bound
T1	-0.014	0.133	-0.019	-0.106	0.916	-0.287	0.258
CMR ^a T2	1.700	1.824	0.349	0.932	0.359	-2.031	5.432
T2*	-3.838	2.178	-0.607	-1.762	0.089	-8.291	0.616
Etiology ^b	-39.330	22.306	-0.378	-1.763	0.088	-84.950	6.291
(Constant)	322.849	151.773		2.127	0.042	12.438	633.260

Dependent Variable: Myocardial Iron Level. a: Measured in Millisecond (msec). b: Non-failing Control (label = 1); Heart failure (label = 2).

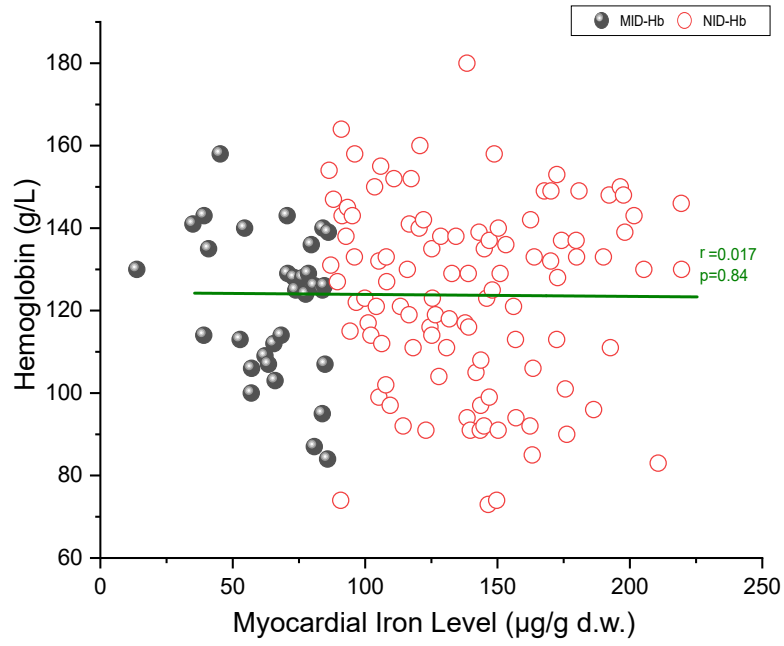
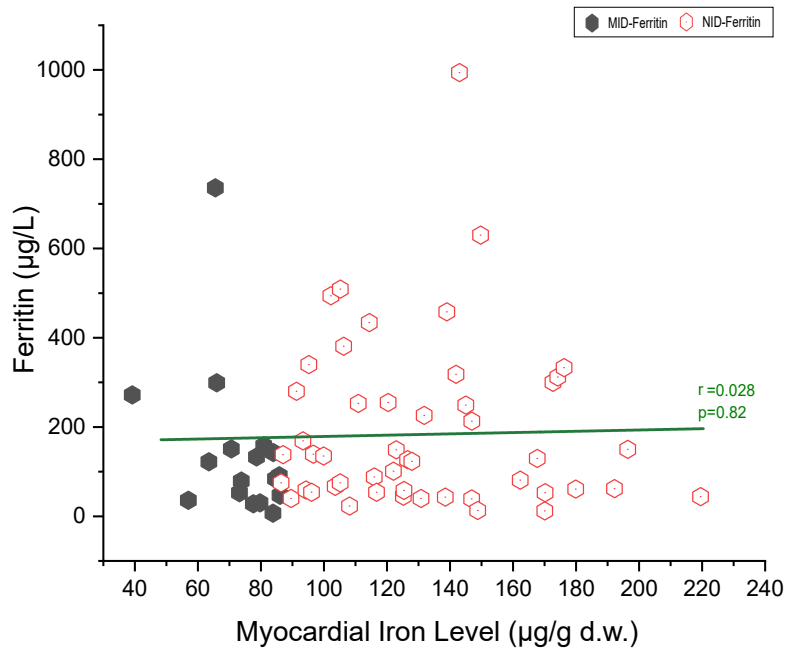
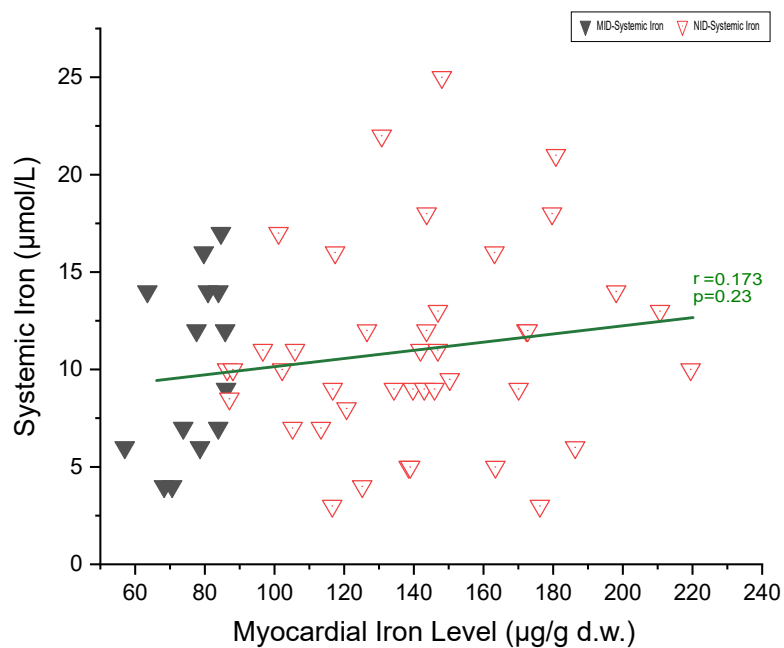
A multiple linear regression was performed, where the myocardial iron level is the outcome variable and the three multiparametric cardiac magnetic resonance mapping (CMR, including T1, T2, and T2*) and one etiological category (1:non-failing control; 2: heart failure) are the predictor variable. The “Enter” method (direct entry) was adopted for the variable selection in the linear regression model. Results show that the overall model could significantly predicted the myocardial iron content by CMR sequences and HF etiology, with $F(4,29)=3.705$ ($p<0.05$, $r=0.581$; **Fig. 6D**). However, only T2* ($\beta=-0.607$, $p=0.089$) and etiology ($\beta =-0.378$, $p=0.088$) are marginally significant predicting variables, whereas T1/T2 does not significantly contribute to the prediction model. More specifically, the myocardial iron levels are predicted to be larger with lower T1 and/or T2* mappings and among healthy individuals. IBM SPSS Statistics for Windows, version 21 (IBM Corp., N.Y., USA) was used for data analysis and narrative interpretation.

Table S3. Basic Clinical Profile of Patients with End-stage Heart Failure Secondary to Dilated Cardiomyopathy (DCM) and Coronary Artery Disease (CAD)

	End-stage HF (N=138)	DCM (N=71)	CAD (N=67)	p-value
Demographic				
Age (years)	54.5 (47.0-61.0)	50.0 (40.0-58.5)	57.0 (48.5-63.0)	<0.001**
Sex, Male	116 (84)	59 (83)	57 (85)	0.751
Heart Weight (gram)	465.0 (374.5-563.0)	476.0 (374.5-546.0)	443.0 (375.5-564.8)	0.928
Comorbidities				
CVD	21 (15)	12 (17)	9 (13)	0.571
PVD	12 (9)	4 (6)	8 (12)	0.189
COPD/Asthma	46 (33)	22 (31)	24 (36)	0.547
DM2	36 (26)	11 (15)	25 (37)	0.004**
Dyslipidemia	41 (30)	12 (17)	29 (43)	<0.001**
Thyroid Disease	22 (16)	14 (20)	8 (12)	0.212
Kidney Disease	74 (54)	39 (55)	35 (52)	0.751
Liver Disease	24 (17)	13 (18)	11 (16)	0.769
Obesity	88 (64)	40 (56)	48 (72)	0.061
PAH	37 (27)	22 (31)	15 (22)	0.254
Hypertension	33 (24)	12 (17)	21 (31)	0.047*
Electrocardiography				
PR Interval (ms)	171.0 (146.0-202.0)	172.0 (148.5-199.0)	168.0 (144.0-205.0)	0.555
QRS Duration (ms)	124.0 (93.0-154.0)	134.0 (102.0-162.0)	112.0 (88.5-148.0)	0.049*
AF	26 (19)	16 (23)	10 (15)	0.253
IVCD	35 (25)	22 (31)	13 (19)	0.118
LBBB	14 (10)	10 (14)	4 (6)	0.115
RBBB	23 (17)	8 (11)	15 (22)	0.080
Blood Parameters				
Ferritin (µg/L)	133.0 (56.0-276.0)	135.0 (62.5-276.0)	110.4 (53.0-261.8)	0.484
Serum Iron (µmol/L)	10.0 (7.0-13.5)	10.0 (6.0-14.0)	11.0 (8.6-12.0)	0.764
TIBC (µmol/L)	54.0 (48.0-67.0)	57.0 (50.0-65.0)	54.0 (47.3-71.5)	0.795
sTF (%)	19.0 (11.3-26.5)	16.0 (11.0-25.0)	20.0 (15.0-27.0)	0.401

Hemoglobin (g/L)	127.0 (109.5-139.0)	133.0 (114.0-142.5)	119.0 (102.0-130.5)	0.001**
MCV (fL)	90.0 (86.0-94.0)	90.0 (86.0-95.0)	90.0 (86.0-93.0)	0.624
MCHC (g/L)	336.0 (328.3-342.0)	336.0 (327.5-341.5)	335.0 (330.0-342.5)	0.465
BNP (pg/ml)	989.0 (485.0-1749.0)	942.0 (494.0-1731.0)	994.5 (476.5-3084.5)	0.624
NT-proBNP (pg/ml)	3671.0 (2677.0-7777.0)	3785.0 (2889.5-8087.0)	2800.0 (1037.8-5100.8)	0.208
C-reactive Protein (mg)	6.5 (3.0-31.8)	7.2 (3.6-42.3)	6.1 (2.6-19.7)	0.472
Creatinine (µmol/L)	121.0 (95.3-150.0)	120.0 (96.5-147.0)	121.0 (93.5-152.5)	0.920
eGFR (ml/min/1.73m ²)	55.0 (41.2-73.5)	55.0 (44.0-75.0)	56.0 (40.0-72.0)	0.529
Medications				
ACEi/ARB	109 (79)	67 (94)	42 (63)	<0.001**
Beta Blocker	112 (81)	61 (86)	51 (76)	0.141
Diuretics	110 (80)	57 (80)	53 (79)	0.864
MRA	80 (58)	48 (68)	32 (48)	0.018*
Digoxin	31 (22)	20 (28)	11 (16)	0.098
Antiplatelet	81 (59)	35 (49)	46 (69)	0.021*
Anticoagulation	97 (70)	54 (76)	43 (64)	0.127
Statin	76 (55)	28 (39)	48 (72)	<0.001**
Antiarrhythmic	61 (44)	37 (52)	24 (36)	0.054

BMI=body mass index; BSA=body surface area; HR=heart rate; SBP=systolic blood pressure; DBP=diastolic blood pressure; NYHA=New York Heart Association Functional Classification; CVD=cerebrovascular diseases; PVD=peripheral vascular diseases; COPD=chronic obstructive pulmonary diseases; DM2=type 2 diabetes mellitus; PAH=pulmonary artery hypertension; AF=atrial fibrillation; IVCD=intraventricular conduction delay; LBBB=left bundle branch block; RBBB= right bundle branch block; TIBC=total iron binding capacity; sTF=saturation of transferrin; MCV=mean corpuscular volume; MCHC=mean corpuscular hemoglobin concentration; BNP=brain natriuretic peptide; NT-proBNP=N-terminal pro b-type natriuretic peptide; eGFR=estimated glomerular filtration rate based on MDRD equation; ACEi=angiotensin converting enzyme inhibitors; ARB=angiotensin receptor blockers; MRA=mineralocorticoid receptor antagonists. Data are presented as means ± standard deviations, medians (with lower and upper quartiles), or numbers (with percentages), where appropriate. Chi-square test, one-way ANOVA (followed by Tukey post hoc analysis) or Mann-Whitney U test were used as appropriate to compare the variables between groups. A two-tailed p value < 0.05 was considered statistically significant, as indicated by an asterisk. *p<0.05; **p<0.01. Categorical variables reported by count with percentage in parenthesis: sex, comorbidities, diagnosis of AF, IVCD, LBBB and RBBB, and medications. Continuous variables reported by median with interquartile range in parenthesis: age, heart weight, PR interval and QRS duration, and blood parameters.

A**B****C****Figure S1**

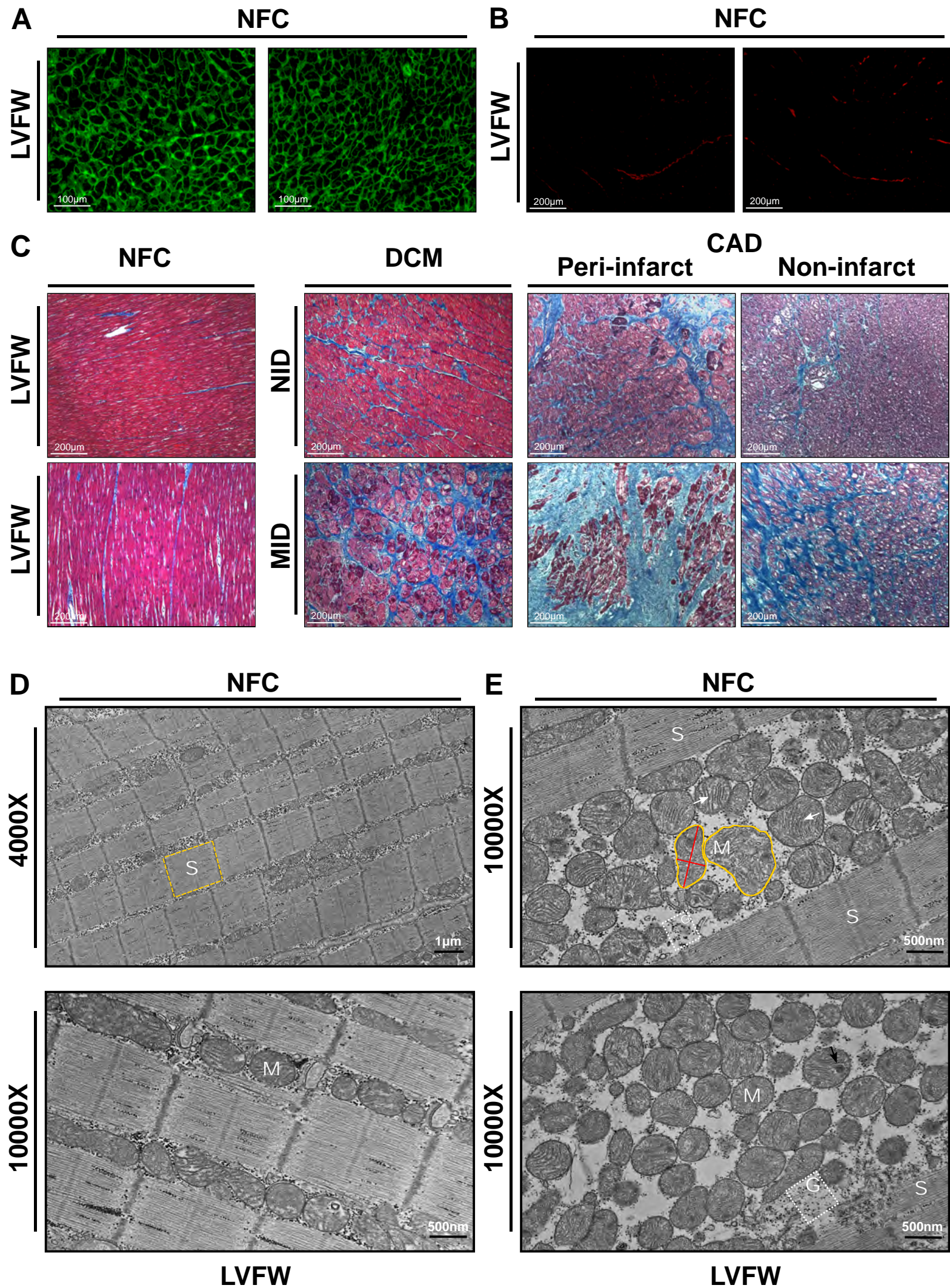


Figure S2

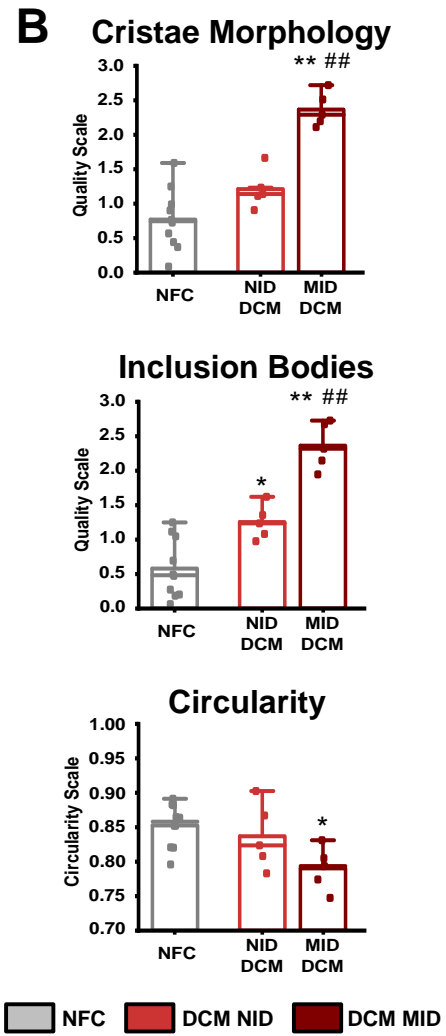
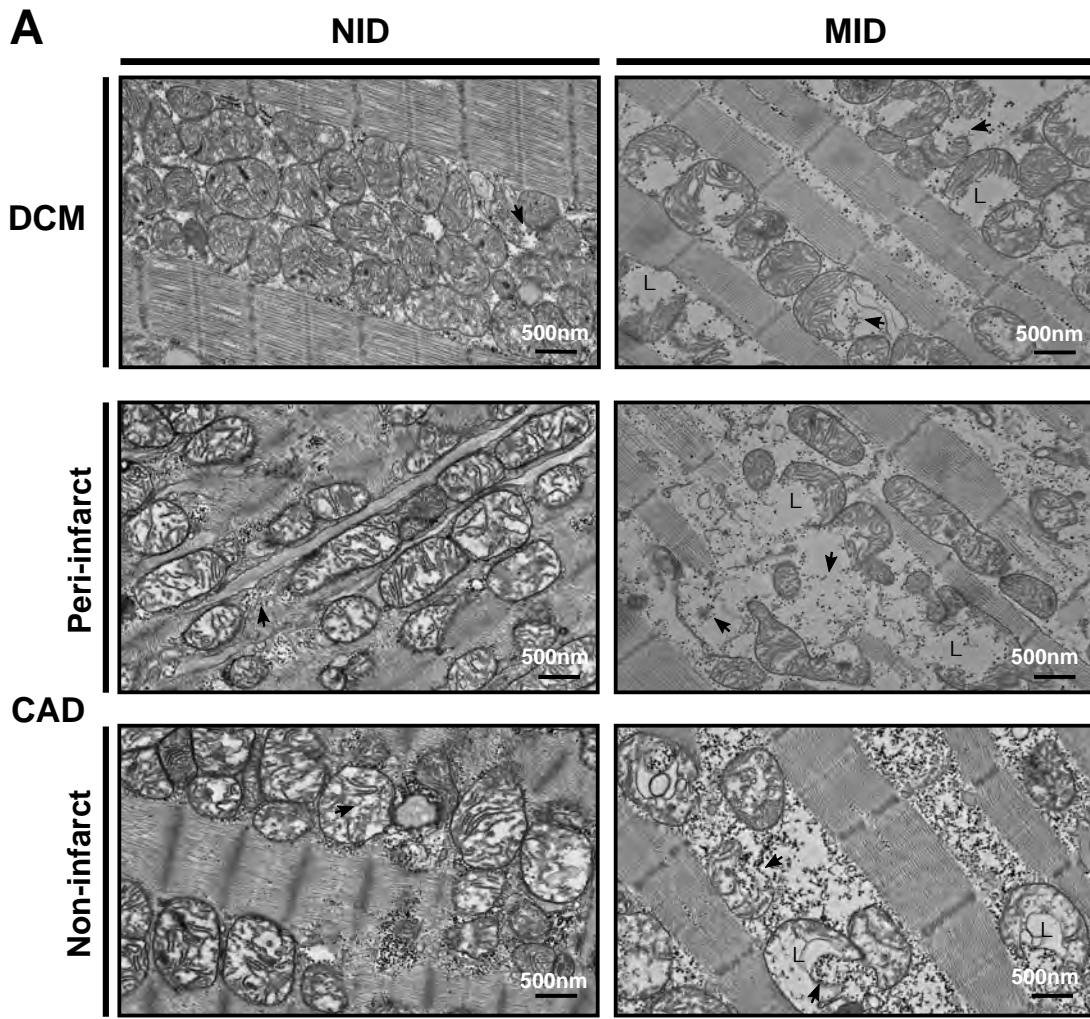


Figure S3

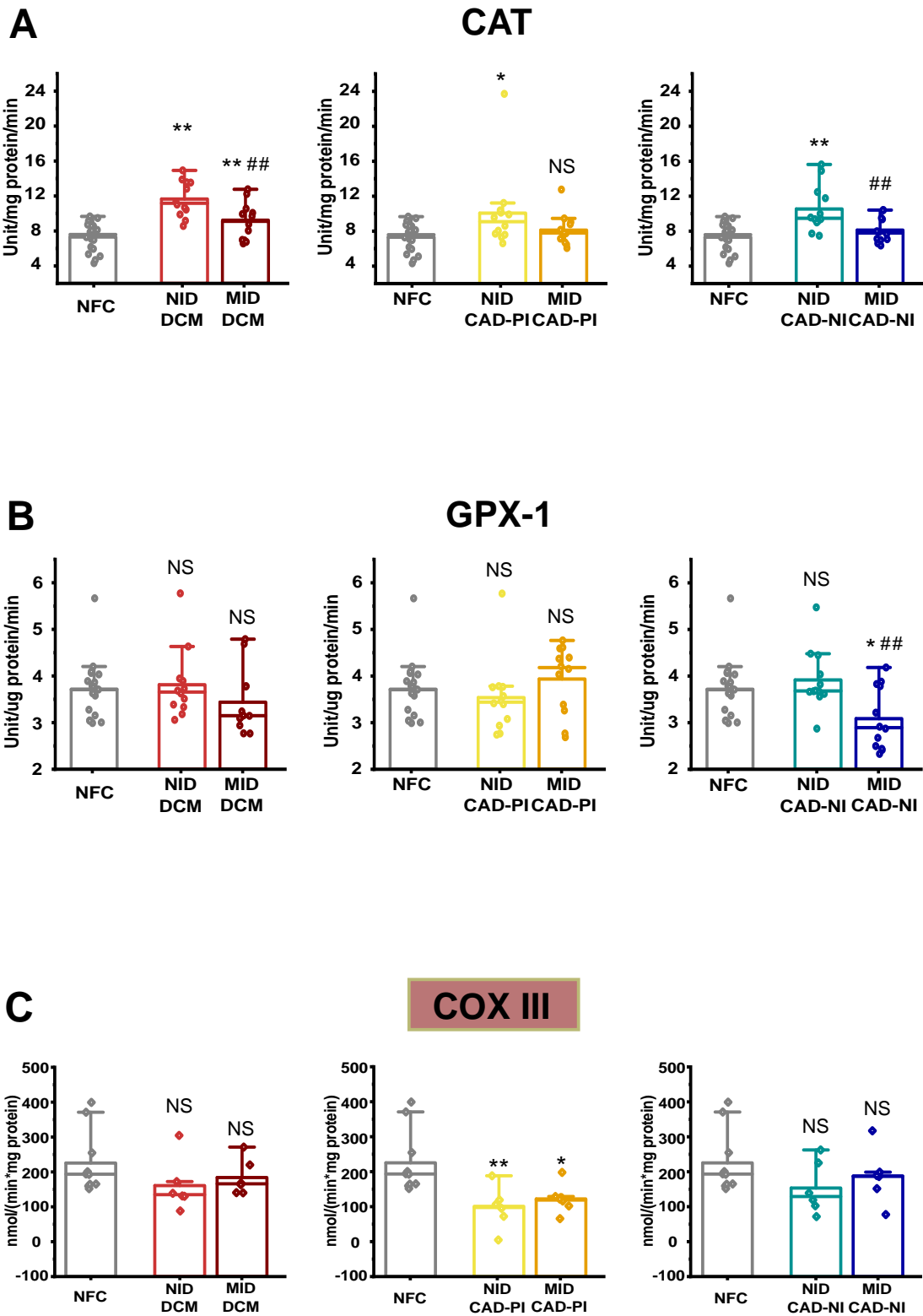
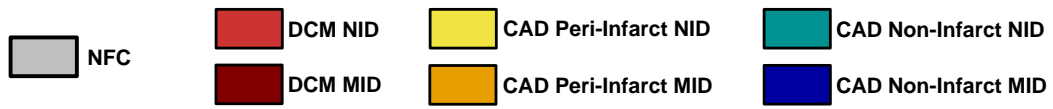
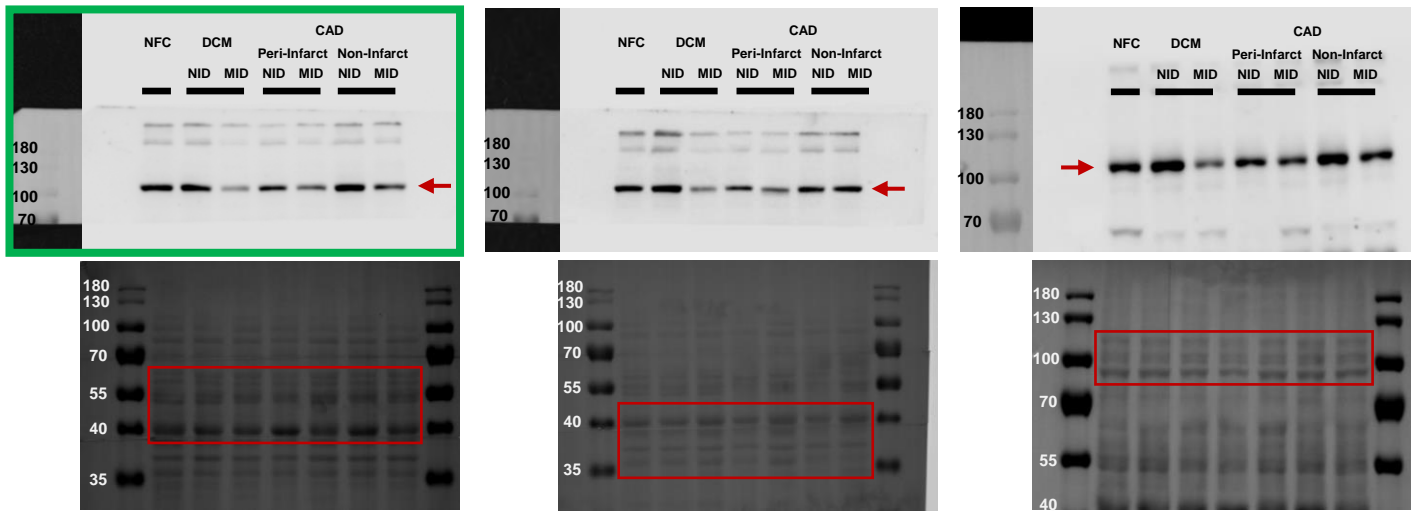


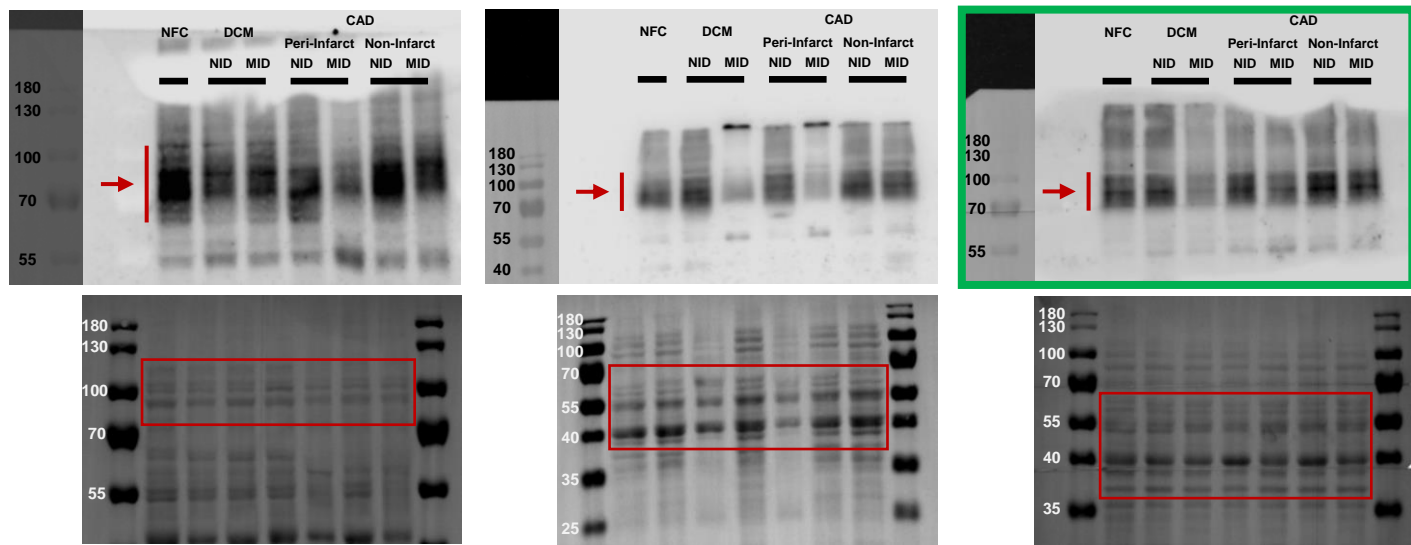
Figure S4

Whole Cell Lysis

TFR-1



DMT-1



FPN

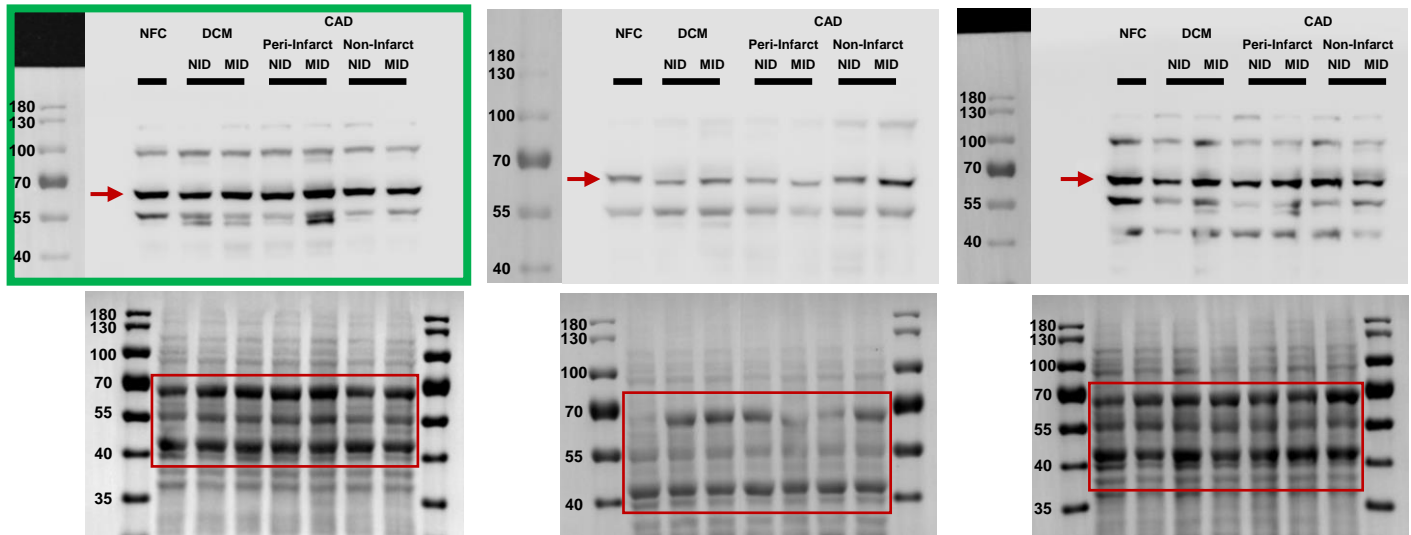


Figure S5

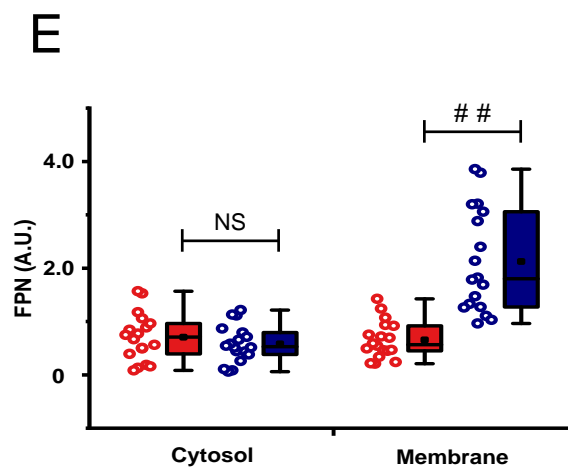
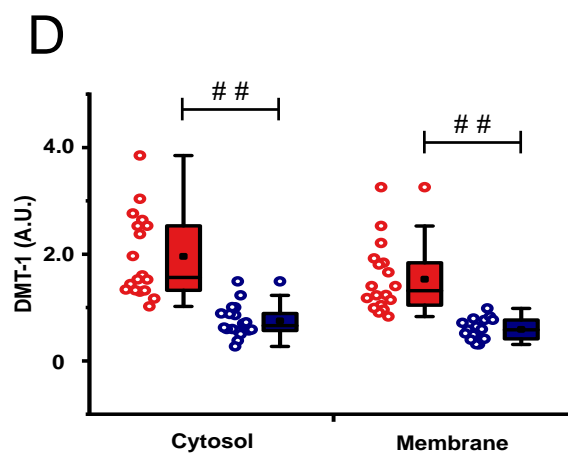
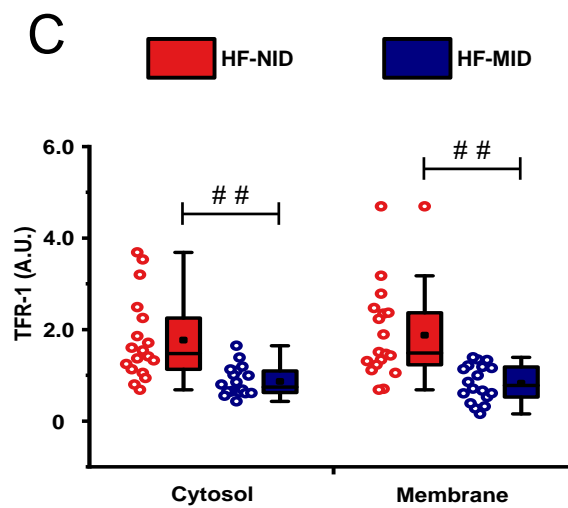
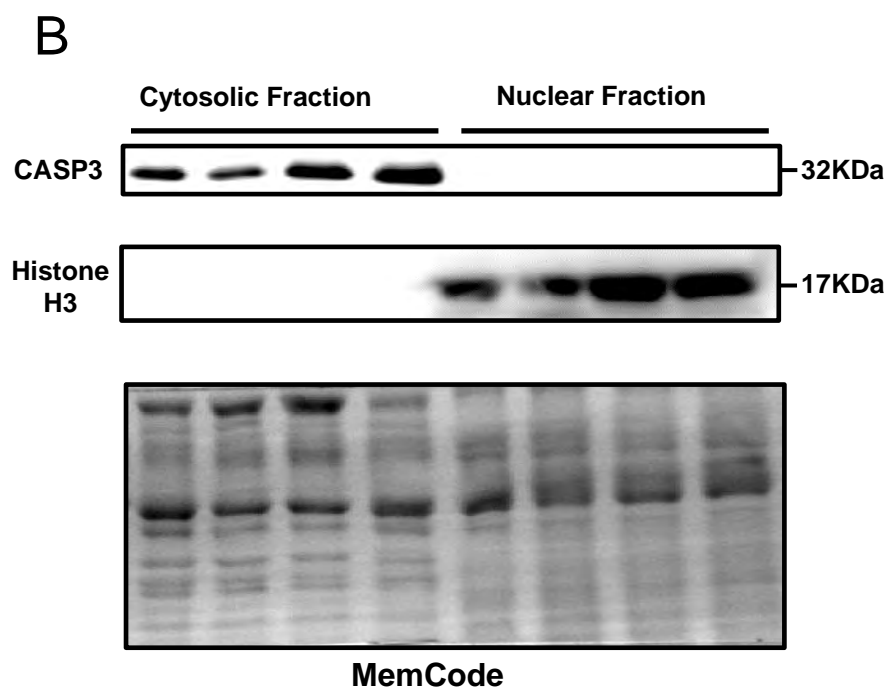
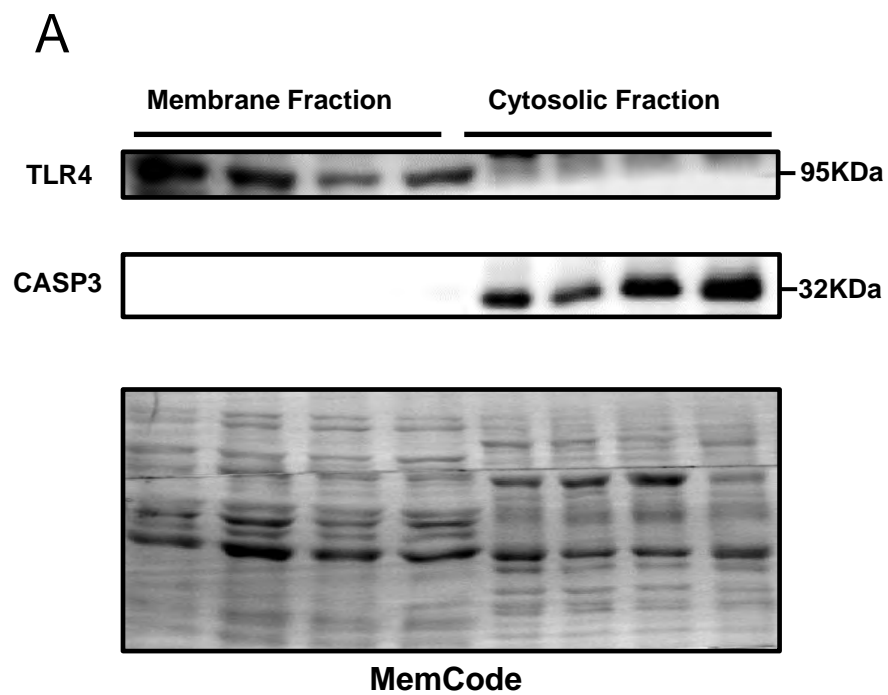
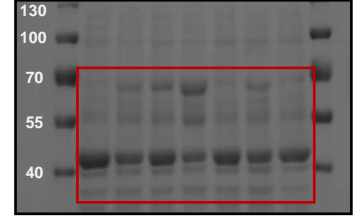
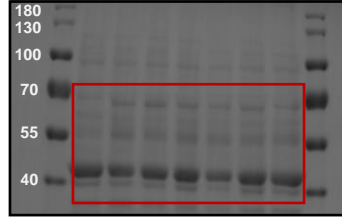
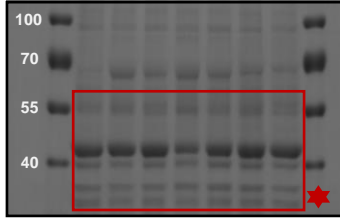
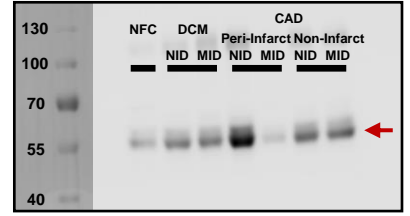
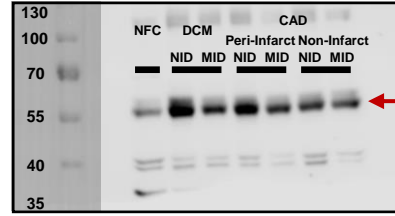
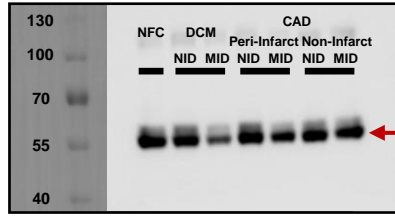
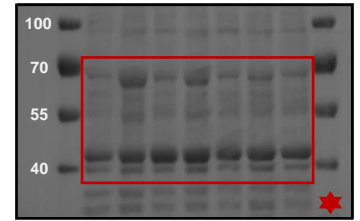
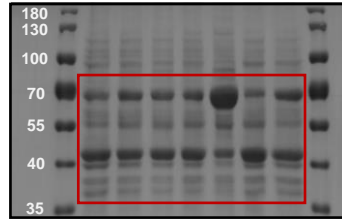
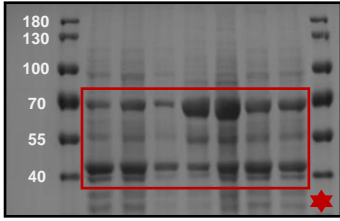
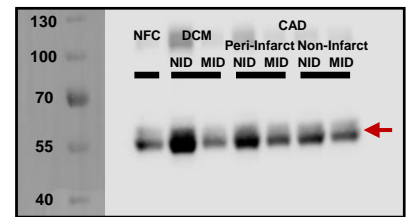
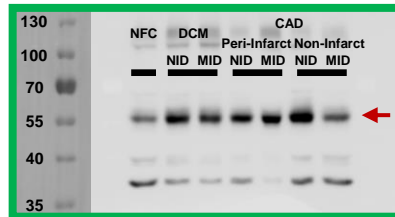
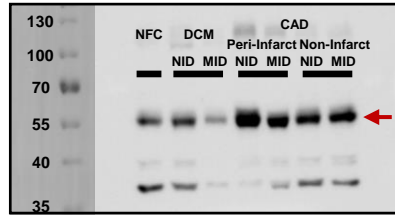


Figure S6

Cytosol



Membrane

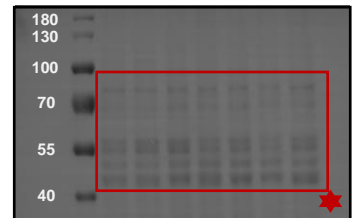
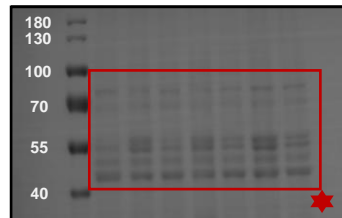
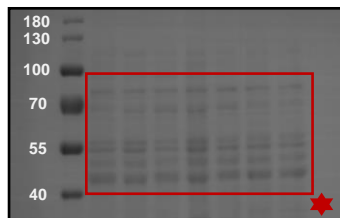
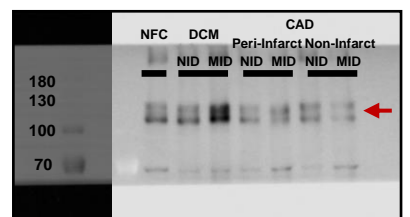
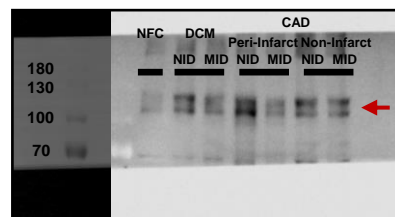
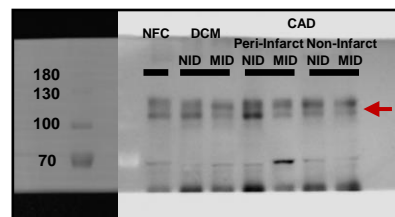
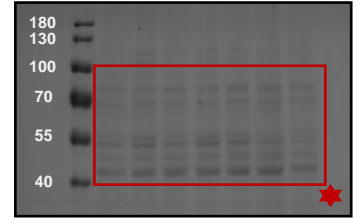
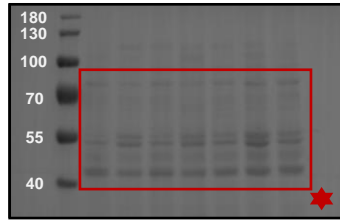
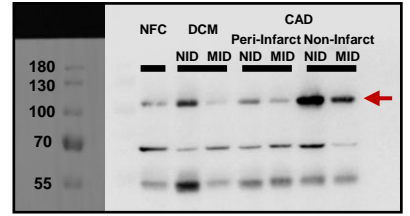
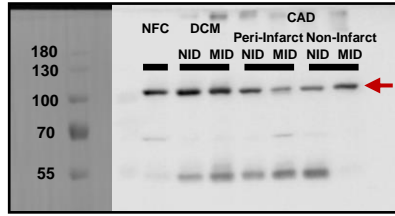
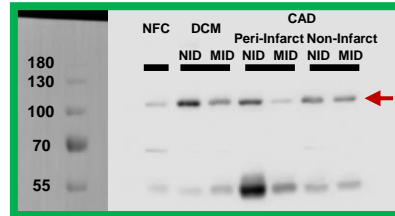
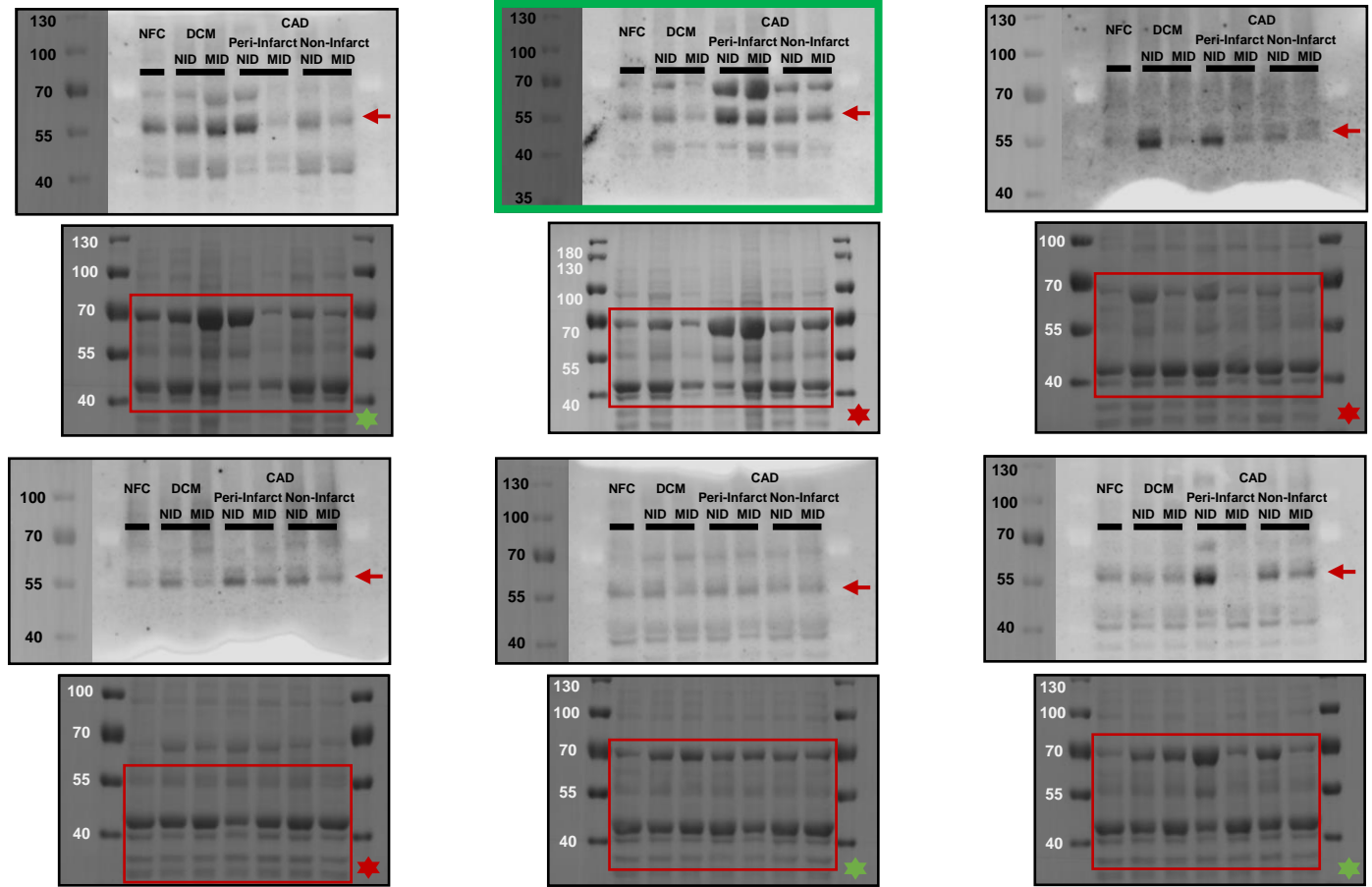


Figure S7

Divalent Metal Transporter 1

Cytosol



Membrane

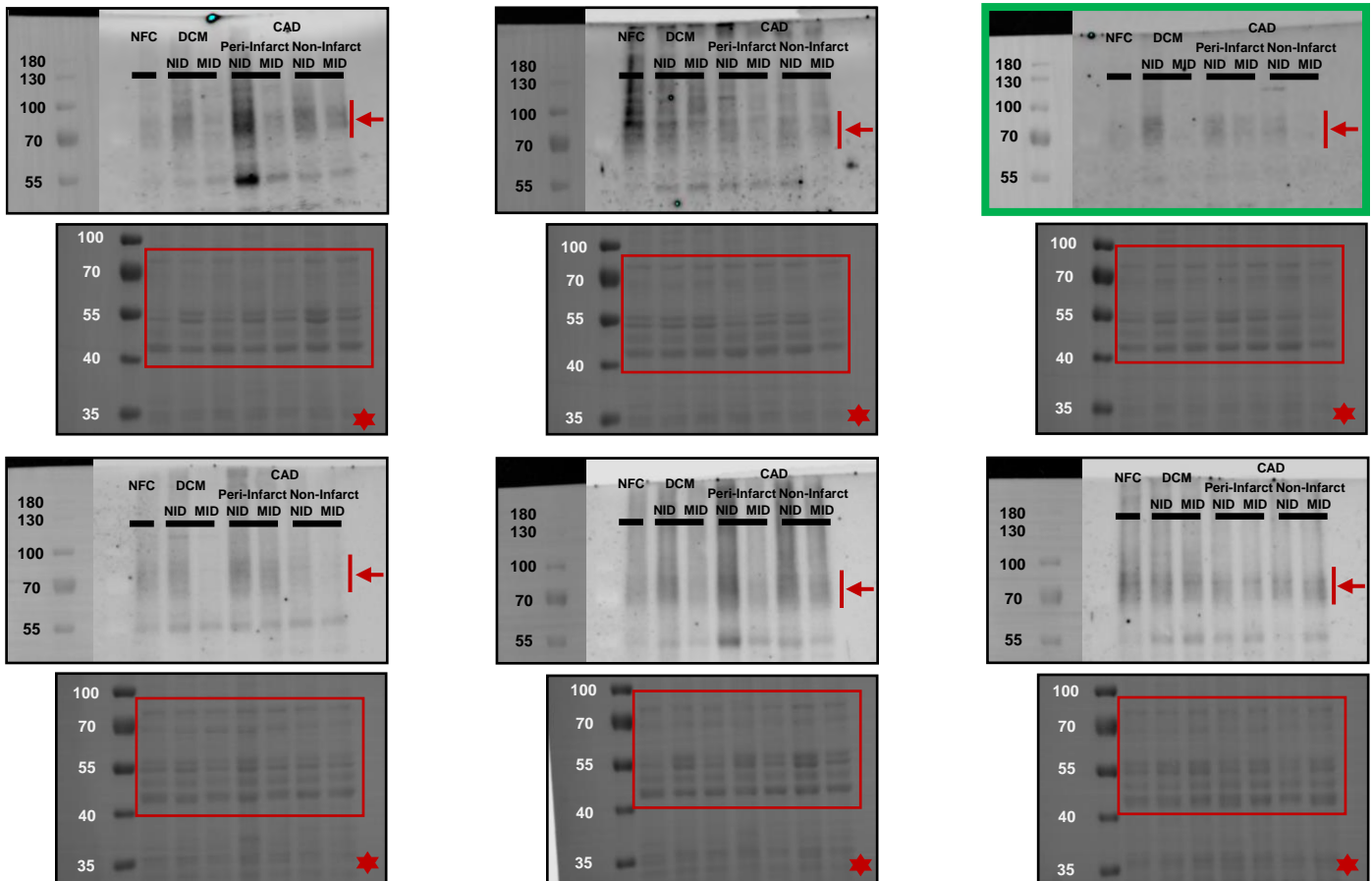
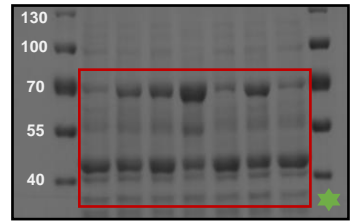
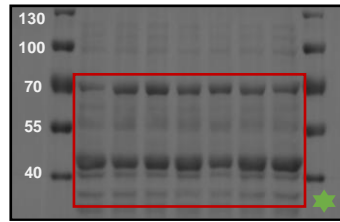
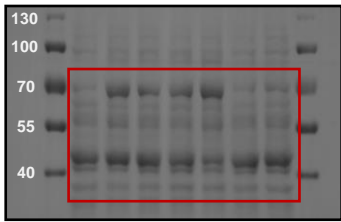
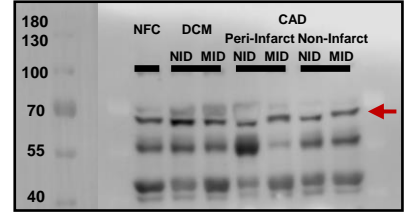
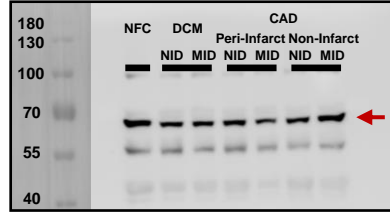
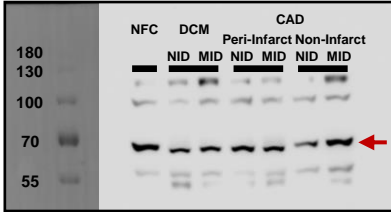
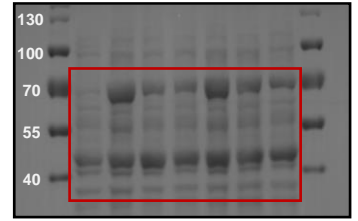
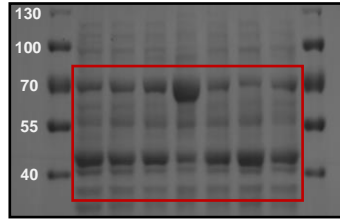
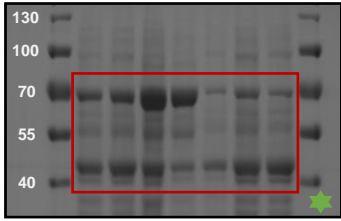
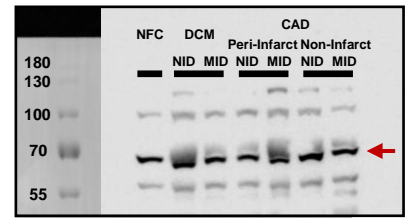
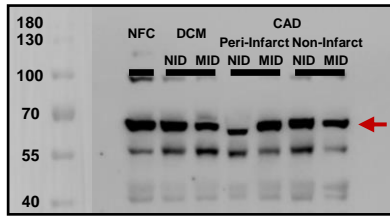
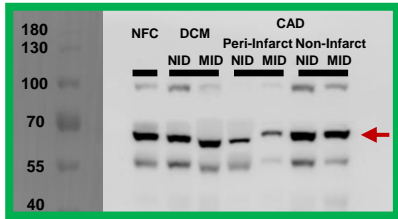


Figure S8

Cytosol



Membrane

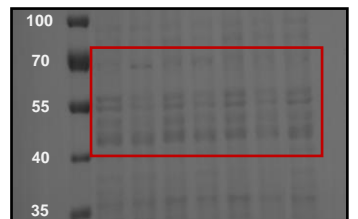
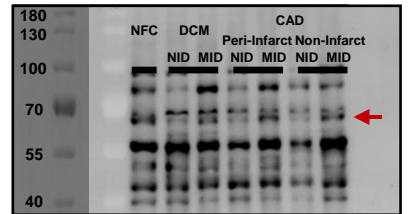
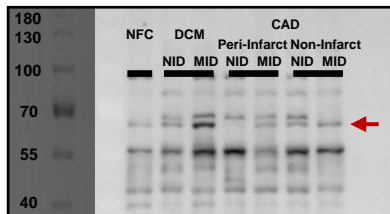
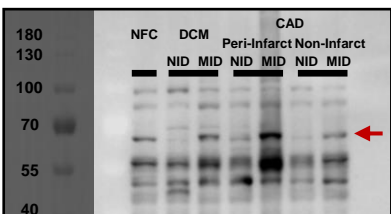
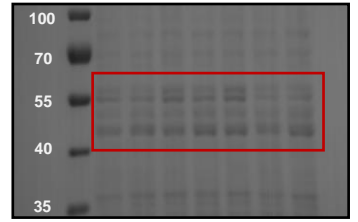
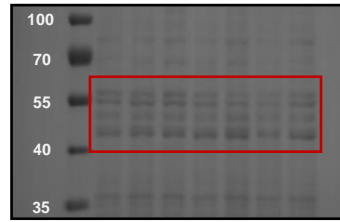
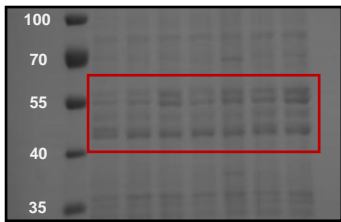
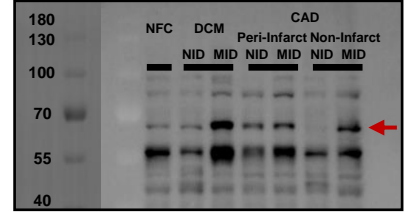
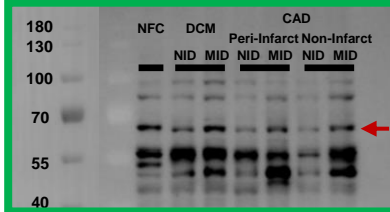
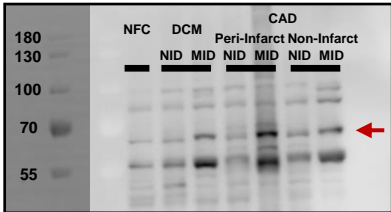


Figure S9

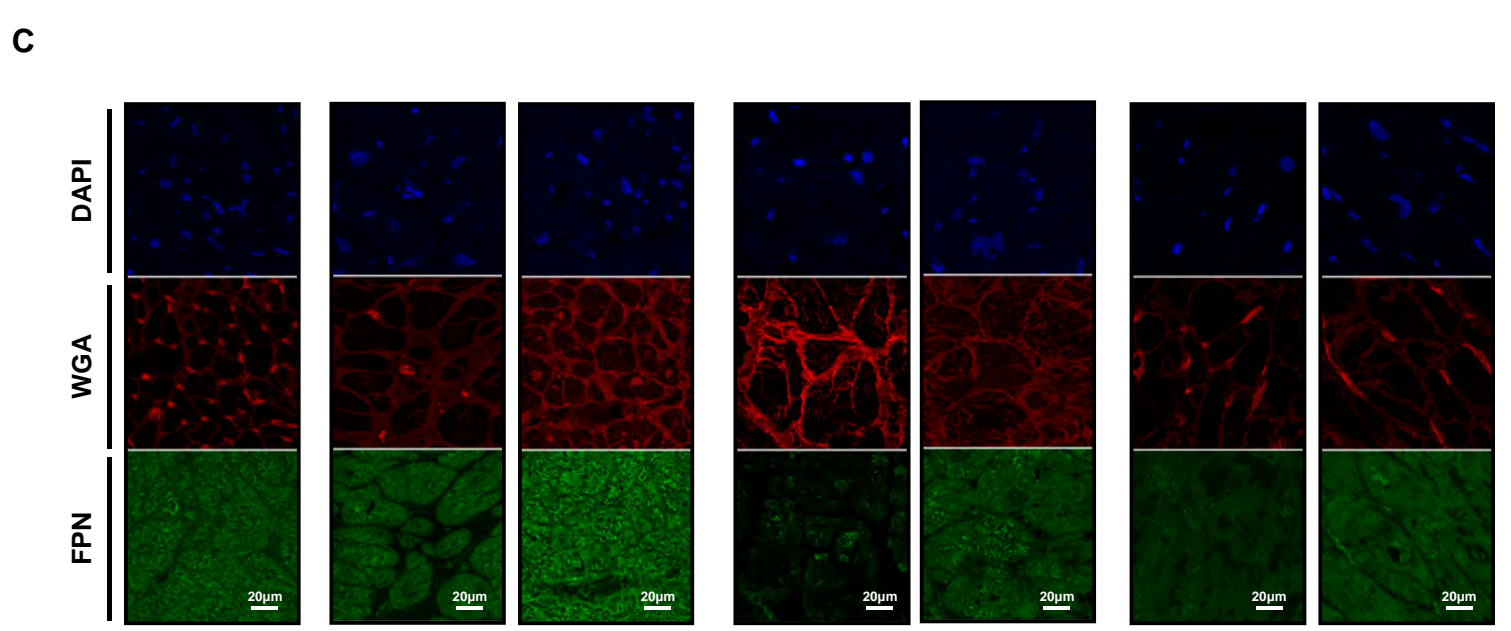
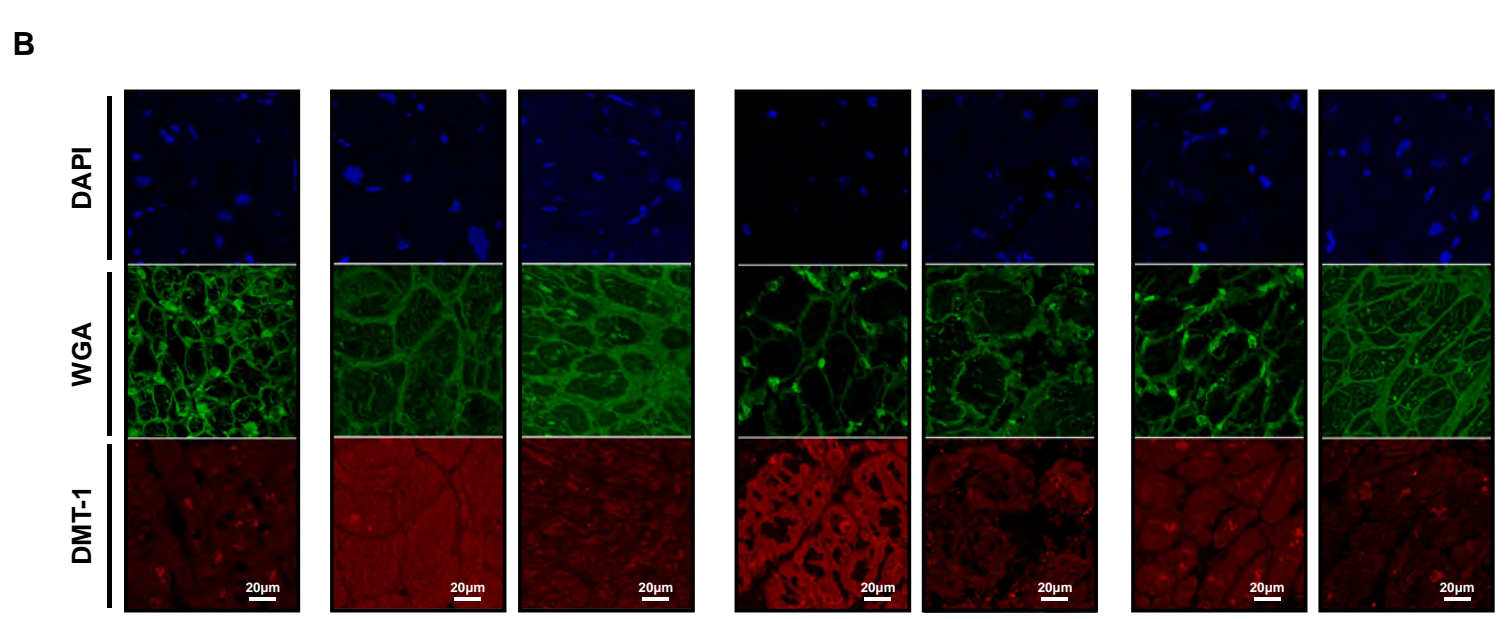
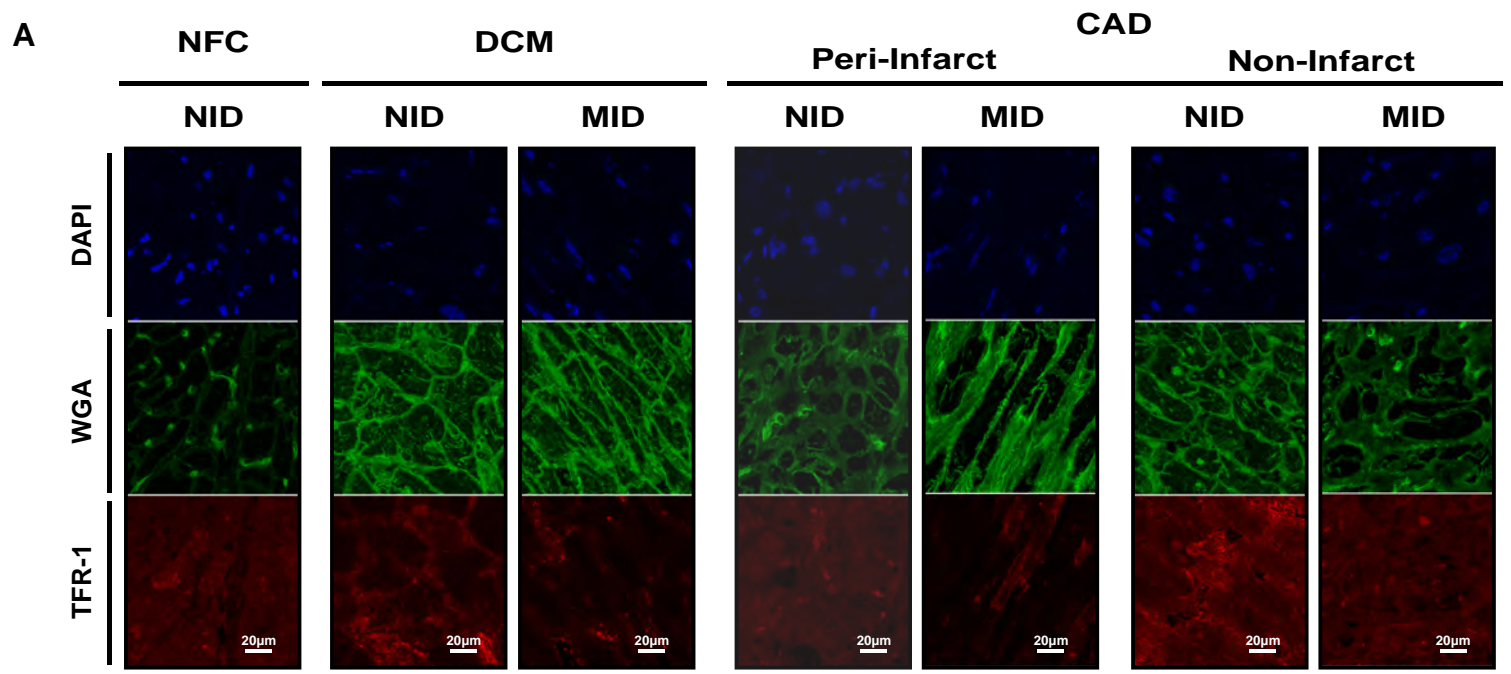


Figure S10

Supplemental Figure Legends

Figure S1. Lack of correlation between myocardial iron levels and systemic hemoglobin (A), ferritin (B), and serum iron (C) levels in HF cohorts, based on linear regression analysis. MID: myocardial iron deficiency, n=32; NID: no myocardial iron deficiency, n=106.

Figure S2. Representative wheat germ agglutinin (A) and picrosirius red staining (B) of normal myocardium (NFC); scale bar = 100 μm (WGA) or 200 μm (PSR). Masson's trichrome staining (C) confirmed exacerbated interstitial fibrosis in the HF subgroups with MID; scale bar = 200 μm . **D-E** Transmission electron microscopy (TEM) images captured from NFC at different magnifications illustrating pristine and well-aligned sarcomeric and mitochondrial ultrastructure; scale bar = 1 μm (4000X) or 500 nm (10000X). S: sarcomere; M: mitochondrion; G: cytoplasmic granules; DCM: dilated cardiomyopathy; CAD: coronary artery disease; LVFW: left ventricle free wall.

Figure S3. Mitochondrial morphological alterations worsened by iron deficiency in failing explanted hearts. Representative TEM images illustrating worsened intra-mitochondrial ultrastructural derangements in iron-deficient failing hearts captured from samples with both DCM and CAD (A) with qualitative quantification shown from the DCM subgroups (B) demonstrating predominant changes in cristae structures and increased presence of inclusion bodies in the MID subgroup with occasional mitochondrial lysis. n=10 for NFC;

n=5 each for DCM-NID and DCM-MID groups. Scale bar = 500 nm. Mito: mitochondria; DCM: dilated cardiomyopathy; CAD-PI: peri-infarcted from coronary artery disease; CAD-NI: non-infarcted from coronary artery disease; NID: no myocardial iron deficiency; MID: myocardial iron deficiency; TEM: transmission electron microscopy. Arrows indicate inclusion bodies. *p<0.05, **p<0.01 compared with NFC; #p<0.05, ##p<0.01 compared with HF-NID.

Figure S4. Enzymatic activities of antioxidant enzymes including catalase (**A**), glutathione peroxidase (GPX-1, **B**) in HF subgroups in comparison with non-failing controls (NFC). n=20 for NFC; n=12 for each HF subgroup. **C.** Enzymatic activity of electron transport chain complex III (COX III) in HF subgroups compared NFC. DCM: dilated cardiomyopathy; CAD-PI: peri-infarcted from coronary artery disease; CAD-NI: non-infarcted from coronary artery disease; NID: no myocardial iron deficiency; MID: myocardial iron deficiency. n=10 for NFC; n=6 for each HF subgroup.

Figure S5. Original immunoblots of iron transporters using whole cell lysates that correspond to the protein quantitation in Figure 5B. TFR-1: transferrin receptor 1; DMT-1: divalent metal transporter 1; FPN: ferroportin. Arrowheads indicated the probed proteins with targeted molecular weight (TFR-1: 100 KDa, DMT-1: 70-100 KDa, FPN: 62.5 KDa), whereas red rectangular boxes showed the part of MemCode that were analyzed for protein abundance normalization. The blots selected as representative in Figure 5B were outlined with a green border.

Figure S6. Western blot analysis demonstrating the validity of our tissue fractionation methods including membrane versus cytosolic (**A**), cytosolic versus nuclear (**B**) fractionations by established compartment-specific markers. **C-E**: Subcellular expression comparisons of TFR-1 (**C**), DMT-1 (**D**), and FPN (**E**) between HF-MID and HF-NID groups, respectively. TLR4: toll-like receptor 4; CASP3: caspase 3. MemCode represents the total protein loading on PVDF membrane. NID: no myocardial iron deficiency; MID: myocardial iron deficiency. n=6 for each HF subgroup.

Figure S7. Original immunoblots of cytosolic and membrane TFR-1 that correspond to the protein quantitation in Figure 5D. TFR-1: transferrin receptor 1. Arrowheads indicated the TFR-1 molecular weight across cytosolic (55 KDa) and membrane (100 KDa) fractions, respectively. Rectangular boxes showed the part of MemCode that were analyzed for abundance normalization, whereas red asterisks indicated those underwent additional membrane stripping and downstream protein redetection (i.e., DMT-1). The blots selected as representative in Figure 5C were outlined with a green border.

Figure S8. Original immunoblots of cytosolic and membrane DMT-1 that correspond to the protein quantitation in Figure 5G. DMT-1: divalent metal transporter 1. Arrowheads indicated DMT-1 molecular weight across cytosolic (55 KDa) and membrane (70-100 KDa) fractions. Rectangular boxes showed the part of MemCode that were analyzed for abundance normalization, whereas colored asterisks indicated those underwent additional

membrane stripping and downstream protein redetection: red asterisks represented the shared MemCode as total protein loading for both TFR-1 and DMT-1 quantification, while green asterisks for DMT-1 and FPN quantification. The blots selected as representative in Figure 5F were outlined with a green border.

Figure S9. Original immunoblots of cytosolic and membrane FPN that correspond to the protein quantitation in Figure 5J. FPN: ferroportin. Arrowheads demonstrated the FPN's unaltered molecular weight in both cytosolic and membrane (62.5 KDa) fractions. Rectangular boxes showed the part of MemCode that were analyzed for abundance normalization, whereas green asterisks indicated those underwent additional membrane stripping and downstream protein redetection (i.e., DMT-1). The blots selected as representative in Figure 5I were outlined with a green border.

Figure S10. Original immunofluorescent images of separated channels that constitute the representative composites of individual iron transporter, including TFR-1 (A, red), DMT-1 (B, red), and FPN (C, green). TFR-1: transferrin receptor 1; DMT-1: divalent metal transporter 1; FPN: ferroportin.